U.PORTO **FEUP FACULDADE DE ENGENHARIA** UNIVERSIDADE DO PORTO **INSTITUTO DE CIÊNCIAS BIOMÉDICAS ABEL SALAZAR** UNIVERSIDADE DO PORTO

i3S INSTITUTO DE INVESTIGAÇÃO E INOVAÇÃO EM SAÚDE UNIVERSIDADE DO PORTO **INEB** Instituto de Engenharia Biomédica

**Dissertation for the
Integrated Masters in Bioengineering**

Thermo-responsive multifunctional nanocomposites for cancer therapy

Francisca Luísa Fernandes Gomes

Supervisors
Prof. Dr. Fernando Jorge Monteiro
Dr. Marta Laranjeira

September 2018

Resumo

O cancro da mama triplo negativo é um dos tipos de doença oncológica mais agressivos atualmente. A quimioterapia é normalmente a melhor opção de tratamento, mas produz efeitos secundários prejudiciais em tecidos como a pele ou o cabelo devido à sua ação inespecífica. Um diagnóstico correto através de procedimentos como a ressonância magnética (RM) pode também prevenir ou monitorizar a doença, ou ainda ajudar ao seu tratamento. Tendo em conta as condições biológicas dos tumores, o desenvolvimento de materiais responsivos a estímulos para entrega controlada de fármacos é uma área promissora na investigação, uma vez que estes conseguem transportar e libertar seletivamente agentes terapêuticos e de diagnóstico.

Neste trabalho, foi desenvolvido um nano-sistema termo-responsivo para quimioterapia direcionada e contraste de RM. Para permitir o contraste de imagem em RM, nano-agulhas de hidroxiapatite dopada com ferro(III) foram sintetizadas e caracterizadas. Para ser usado como veículo de transporte, um microgel polimérico termo-responsivo foi também sintetizado e caracterizado, com um núcleo de poli[(N-isopropilacrilamida-co-2-(dimetilaminoetil metacrilato)] [P(NIPAM-co-DMAEMA)] e um revestimento de poli[(N-isopropilacrilamida-co-poli(etilenoglicol) metacrilato] [P(NIPAM-co-PEGMA)]. As nano-agulhas mostraram comprimentos de 20-80 nm e larguras entre 6 e 18 nm. Registou-se ainda uma carga de superfície de –(33.0 ± 0.9) mV. Quimicamente, as agulhas mostraram a presença de pequenas fases de fosfato tricálcico e óxidos de ferro. As agulhas não-sinterizadas provaram ser paramagnéticas, enquanto as sinterizadas mostraram superparamagnetismo e ferrimagnetismo. O microgel registou tamanhos abaixo dos 200 nm e uma temperatura de transição de volume média de 38.6°C. Adicionalmente, foi testada a encapsulação das nano-agulhas, sem sucesso, e do fármaco quimioterapêutico doxorubicina no polímero, este com melhor resultado. Destacam-se os seus valores da eficiência de encapsulação (75.6%) e capacidade de carga (9.1%). Por último, ensaios de atividade metabólica em fibroblastos gengivais humanos incubados com microgéis não demonstraram reduções na viabilidade celular.

Em suma, neste trabalho foi desenhado e caracterizado um sistema multifuncional bastante promissor. Estudos futuros deverão focar-se na junção de todos os componentes – nano-agulhas superparamagnéticas, doxorubicina e microgel – e testados os perfis de libertação de fármaco e viabilidade celular em linhas cancerígenas. A encapsulação de ácidos nucleicos poderá também abrir portas para uma nova funcionalidade: a terapia genética através de entrega controlada de genes.

(page intentionally left blank)

Abstract

Triple negative breast cancer is one of the most aggressive oncological conditions currently known. Chemotherapy is usually the best treatment option, although with deleterious side effects in tissue such as skin or hair, resulting from its unspecific action. Correct diagnosis through procedures such as magnetic resonance imaging (MRI) can prevent and monitor disease and also aid treatment. Having in mind the biological conditions of tumours, namely high temperatures, stimuli-responsive materials for controlled drug delivery are a promising area of research due to their ability to carry and selectively release both therapeutic and diagnostic agents.

In this work, a thermo-responsive composite nano-system for targeted chemotherapy and MRI contrasting was designed. For the diagnostic functionality, iron(III)-doped hydroxyapatite (FeHAP) nano-needles were synthesized and characterized. For the nanocarrier, a thermo-responsive polymeric core-shell microgel made of poly[(N-isopropylacrylamide-co-2-(dimethylaminoethyl methacrylate)] [P(NIPAM-co-DMAEMA)] as the core and poly[(N-isopropylacrylamide-co-poly(ethylene glycol) methacrylate] [P(NIPAM-co-PEGMA)] as the shell was also synthesized and characterized. The nano-needles yielded lengths between 20-80 nm and widths between 6-18 nm. Surface charges of –(33.0 ± 0.9) mV were also reported. Chemically, the sample showed the presence of small tricalcium phosphate, magnetite and maghemite formations. Non-sintered FeHAP proved paramagnetic while sintered FeHAP showed both superparamagnetic and ferrimagnetic behaviour. The polymeric nanocarrier showed sizes below 200 nm and an average volume phase transition temperature of 38.6°C. Attempts at encapsulating both nano-needles and chemotherapeutic drug doxorubicin (DOX) into the polymeric nanocarrier were performed but not successful in the case of FeHAP. For DOX, remarkable encapsulation efficiency (75.6%) and loading capacity (9.1%) were registered. Lastly, metabolic activity assays were conducted in human gingival fibroblasts (HGF), cultured in the presence of these core-shell microgels, with no reduced viability.

To conclude, a promising multifunctional system was hereby developed and characterized. Further studies should consider the final assembly of superparamagnetic nano-needles, DOX and microgels, along with drug release profile and cancer cell viability studies. Finally, nucleic acid encapsulation would take advantage of yet another promising functionality of this nanocarrier – controlled gene delivery and therapy.

I never dreamed about success. I worked for it.

- Estée Lauder

Acknowledgements

First of all, I would like to thank all the Biocomposites team, especially my supervisor Prof. Dr. Fernando Jorge Monteiro and co-supervisor Dr. Marta Laranjeira for providing me with everything necessary to my work, sharing their knowledge and supporting my ideas.

Secondly, my most honest appreciation goes to Prof. Dr. Patrick van Rijn, Dr. Philipp Kühn and Dr. Olga Mergel. It is thanks to them that my interest sparked for an area of which I knew very little but had much fun learning. Thank you for providing me with such abundant knowledge, material, and new perspectives.

To Prof. Dr. Joaquim Agostinho Moreira and Prof. Dr. Abílio Almeida, thank you for showing the importance of physics in medicine and so patiently introducing me to new concepts.

I sincerely thank Dr. André Pereira for his dedication and willingness to help by sharing valuable knowledge and useful tools, not just during my master's dissertation but also throughout my masters degree.

To Rui Vilarinho and Fábio Figueiras, thank you for helping me with material characterization and for clarifying many aspects of my work.

To Ricardo Vidal, Dalila Pedro, Rui Fernandes, Ana Malheiro and Fátima Fonseca, thank you for providing me with valuable advice and training in the equipment at i3s. Much of my characterization work would not be done without you.

To Marco Araújo and Vicky Leiro Rodríguez, thank you for your help in clarifying my immediate questions regarding polymer chemistry.

Now, to my parents, thank you for listening to me when nothing seemed to work. Thank you for giving me guidance and motivation, not just now but through life.

To my friends, thank you for your everyday support; mutually sharing concerns and small victories helped us all through these troubled times.

To Daniel, an endless thank you for your help, in every aspect. For listening to my concerns every day from start to finish and for teaching me things of which I would not have ever dreamt I did not know. Thank you.

(page intentionally left blank)

Contents

(page intentionally left blank)

List of Figures

(page intentionally left blank)

List of Tables

(page intentionally left blank)

List of Abbreviations

ADMET	*Administration – Distribution – Metabolism – Excretion - Toxicity*
APS	*Ammonium persulfate*
ATRF	*Atom Transfer Radical Polymerization*
Bis	N,N-methylenebisacrylamide
CT	*Computerized Tomography*
DDS	*Drug delivery systems*
DLS	Dynamic light scattering
DMAEMA	*2-(Dimethyl aminoethyl) methacrylate*
DMAPMA	*N-[3-(dimethylamino)propyl] methacrylamide*
DNA	*Deoxyribonucleic acid*
EGF	*Epidermal Growth Factor*
EGFR	*Epidermal Growth Factor Receptor*
EPR	*Enhanced Permeation and Retention*
ER	Estrogen receptor
(US) FDA	*(United States) Food and Drug Administration*
FeHAP	*Iron(III)-doped hydroxyapatite*
FRP	*Free Radical Polymerization*
FTIR	*Fourier Transform Infrared Spectroscopy*
HAP	*Hydroxyapatite*
HER2	*Human Epidermal Growth Factor Receptor 2*
KPS	*Potassium persulfate*
LCST	*Lower Critical Solution Temperature*
mAb	*Monoclonal antibody*
MEMS	*Microelectrical Mechanical Systems*
MRI	Magnetic Resonance Imaging
Ms	*Saturation magnetization*
MWCO	*Molecular weight cut-off*
nanoHAP	*Nanohydroxyapatite*
NIPAM	*N-(Isopropylacrylamide)*
NIR	*Near-infrared*
PAA	*Poly(acrylic acid)*
PdI	*Polydispersity index*

PDMAEMA	*Poly(dimethylaminoethyl methacrylate)*
PEG	*Poly(ethylene glycol)*
PEGMA	*Poly(ethylene glycol) methacrylate*
PET	*Positron emitted tomography*
PGMA	*Propylene glycol methacrylate*
PHEMA	*Poly(2-hydroxyethyl methacrylate)*
PLGA	*Poly(lactic-co-glycolic) acid*
PMAA	*Poly(methacrylic acid)*
PMMA	*Poly(methyl methacrylate)*
PNIPAM	*Poly(N-Isopropylacrylamide)*
PR	Progesterone receptor
RAFT	*Reverse Addition–Fragmentation Chain-transfer Polymerization*
RES	*Reticuloendothelial System*
ROS	*Reactive oxygen species*
RNA	*Ribonucleic acid*
SDS	*Sodium dodecyl sulphate*
SEM	*Scanning electron microscopy*
SPIONS	*Superparamagnetic Iron Oxide Nanoparticles*
TCP	*Tricalcium phosphate*
TE	*Echo Time*
TEM	*Transmission electron microscopy*
TNBC	*Triple negative breast cancers*
TR	*Repetition Time*
UV	*Ultraviolet*
VEGF	*Vascular Endothelial Growth Factor*
VPF	*Vascular Permeability Factor*
VPTT	*Volume Phase Transition Temperature*
XRD	X-ray Diffractometry

(page intentionally left blank)

(page intentionally left blank)

Chapter I

Introduction

1.1. Cancer

1.1.1. Epidemiology

In present times, cancer is one of the most common medical conditions worldwide, only overpassed by heart disease.(1) In 2015, cancer was responsible for approximately 600,000 deaths in the US, and nearly 8.8 million worldwide, which translates into 1 in 6 deaths globally.(2) Many advances in oncology have been recently made, contributing to the reduction of the mortality rates - in the period of 2005-2014, cancer death rates were reduced 1.5% annually, and 25% in the overall period from 1991 to 2014.(3)

Breast cancer accounted for 1.7 million diagnostics in 2012 and is the most common type of cancer in women, reporting a staggering 25% of all cancers.(4) They can be categorized according to their expression of three main receptors – estrogen receptor (ER), progesterone receptor (PR), and human epidermal growth factor receptor 2 (HER2). The kind that does not express any of these receptors is aptly named triple negative breast cancer (TNBC) and is currently the object of study of many research groups. Dent conducted a study in which 11% of breast cancer patients suffered from TNBC and reported that their five-year survival rates were lower than for any other types of breast cancer, with the addition of a high risk of distal recurrence and a rapid progression from this recurrence to death.(5) It is, unarguably, one of the most aggressive types of breast cancer.

1.1.2. Tumor biology

Neoplasms, or tumours, were defined by well-known pathologist W.H. Clarke in 1991 as populations of "abnormal cells showing temporally unrestricted growth preference over their normal counterparts. Such abnormal cells invade surrounding tissues, traverse at least one basement membrane, grow in the mesenchyme at the primary site, and may metastasise to distant sites."(6)

Cancerous cells can proliferate in the bloodstream or, more commonly, assemble into solid masses. In the latter case, two different parts can be identified: a) the *parenchyma*, which consists in the mass of abnormally grown cells, and b) the *stroma*, which consists of the extracellular matrix, a basement membrane, blood vessels that irrigate the site, and other cells such as bone marrow-derived cells, tumour-associated macrophages or carcinoma-associated fibroblasts.(7) The biochemical crosstalk between the plethora of different cells in the stroma and the parenchyma contributes to the establishment of the primary tumour site and of pre-metastatic niches in other sites, all favourable to cell proliferation. These frequently translate into immunosuppression, chronic inflammation, extracellular matrix constant restructuring with the alternated cleavage and growth of collagen fibers, and most notably the development of new blood vessels – angiogenesis (Fig.1).
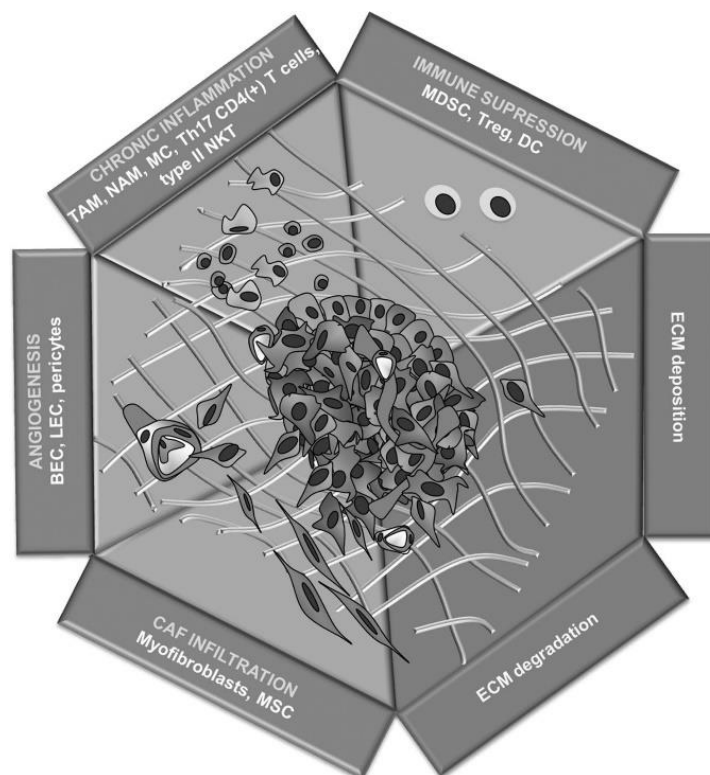
Figure 1. Cellular processes involved in the establishment of the tumour microenvironment. Chronic inflammation, immune suppression, extracellular matrix deposition and degradation, fibroblast infiltration and angiogenesis contribute to the maintenance of the parenchyma and the stroma. Source: Sounni et al. (2013).(8)

Indeed, fast cell proliferation is linked to a rampant need for oxygen, nutrients and growth factors. Cancer cells naturally adapt by overexpressing a number of growth factors receptors, usually present in healthy cells – vascular permeability factor (VPF), vascular endothelial growth factor (VEGF), folic acid, transferrin or epidermal growth factor (EGF) receptors, as well as integrins αβ3 or αβ5, are some examples.(9-11) Triple negative breast cancer cells, for instance, are thought to commonly overexpress the epidermal growth factor receptor (EGFR).(5) Two other interesting adaptation phenomena are poor lymphatic drainage and the fact that newly-formed blood vessels tend to have disorganized structures and wide fenestrations of 100-780 nm, responsible for their abnormal permeability.(12) The combination of both events was named enhanced permeability and retention (EPR) effect, and has proven useful for therapies that involve drug delivery to the tumour site.

Tumours can be classified as benign or malignant. The main factor of differentiation between both is the presence and integrity of the basal membrane - while benign tumours are contained within this barrier, malignant tumours are able to break it with the action of collagenases and other cleaving proteins, allowing cell extravasation to the bloodstream and other organs - metastasis.(13) Depending on the type and location of the tumour, cells tend to metastasize to specific organs - breast cancer cells, for instance, tend to invade bone, lungs, lymph nodes, brain or the liver, but more frequently to bone.(14) TNBCs, however, do not follow the bone tendency and tend to metastasize to lung and viscera.(5)

As would be desirable for the treatment of cancer, cells can undergo programmed death – apoptosis - under certain stress conditions. During the disruption of apoptosis regulatory pathways in cancer cells, the mitochondria releases pro-apoptotic factors into the cytosol to stimulate the activation of several protein complexes, which will in turn trigger cell death. Possible causes include intracellular calcium (Ca^{2+}) imbalance, DNA-damaging factors such as the chemotherapeutic drugs doxorubicin and cisplatin(15, 16) or oncogene factors.(17, 18) Cell-cycle arrest can also reduce the proliferation rates and may be induced by gamma irradiation, drugs such as methotrexate, or more recently discovered, nanohydroxyapatite.(19-21)

1.1.3. Cancer Diagnostics

The general cycle of care starts by an appointment with a physician, who detects a possible risk and advises either a) lab tests to urine, blood, or other body fluids; b) imaging analysis; or c) biopsy followed by pathological analysis.(22) If a cancer diagnosis is confirmed, staging of the disease is then determined and the specialized physician responsible for the patient is duly informed, so as to decide on the best treatment.

Bioimaging is generally used in the study of small or deeply-located tumour masses, possible through positron emission tomography (PET), magnetic resonance imaging (MRI), computer tomography (CT), or ultrasound.

Magnetic resonance imaging is a technique which entails the application of a strong magnetic field (0.3 to 1.5 T) to a living organism for organ visualization. The main advantages of MRI rely on excellent spatial resolution, high sensitivity, non-invasiveness and radiation-free mode of action, which is especially important for the prevention of mutagenesis and, consequently, tumour formation. Limitations of MRI are the fact that it is rather expensive, cannot be used in patients with implantable metal-containing devices, and requires specialized units within hospitals.(23)

Briefly, in MRI, the hydrogen atoms of water molecules are able to align with the magnetic field as magnetic dipoles while absorbing and emitting specific pulsed radio frequencies. As soon as the pulse is turned off, the protons emit radio waves at different rates, according to the chemical composition of their surroundings (tissue relaxation time).(23) Tissue relaxation times can be classified as T1 (longitudinal or spin-lattice) or T2 (transverse or spin-spin).(24) Different imaging modalities can be chosen, of which T1- or T2-weighted images. In T1-weighted, water usually appears darker while fat and paramagnetic contrast agents (such as gadolinium chelates) appear lighter.(25) On other hand, in T2-weighted images, water will appear brighter while fat and superparamagnetic contrast agents (such as magnetite nanoparticles) will appear darker.

Contrast agents are an important addition on MRI, especially when small and/or deep tissue tumours are suspected. Due to their nanoscale size, oftentimes through the EPR effect, they are retained in the tumour sites and can enhance the contrast of the final image so as to help doctors in future procedures, like tumour excision surgeries. Much research has been done on the enhancement of the biocompatibility of MRI contrast agents, as described in future sections.

1.1.4. Cancer Treatments

Common kinds of cancer treatment include surgery, for excision of the carcinogenic mass; chemotherapy, which is employed through the administration of drugs that reduce cell proliferation by disturbing its survival mechanisms; radiotherapy, which entails the irradiation of carcinogenic tissue to induce cell death; or hormonal therapy, for inhibition of the binding of certain hormones to their receptors (e.g. estrogen in estrogen receptor-positive breast cancers). Novel approaches include targeted therapy, a treatment especially directed towards tumour cells instead of healthy ones. Some targeted approaches include hormonal inhibitors, monoclonal antibodies, or surface-modified nanoparticles as targeted carriers of chemotherapy drugs (Table 1).(26) Non-

targeted treatments affect all types of tissue indiscriminately – healthy hair follicles, bone marrow cells and cells of the digestive system - possibly resulting in hair loss, anemia, or nausea.(27) Targeted therapies have, thus, partly arisen from this need to reduce side effects.

Breast, prostate or ovarian cancer are usually composed of cells which overexpress hormone receptors, and thus can be treated with adequate hormone-based drugs such as lapatinib, tamoxifen or exemestane (Table 1). Triple negative breast cancers (TNBC), however, do not express any of the three hormonal receptors for estrogen (ER), progesterone (PR) or human epidermal growth factor receptor 2 (HER2), and so cannot be treated in this way. Along with other metastasized breast cancers, they commonly undergo more aggressive chemotherapeutic treatments with doxorubicin or paclitaxel.

The problem of chemotherapy drugs circulating freely in the bloodstream is non-specific cell death. Furthermore, most drugs are rather insoluble in water and exhibit fast renal clearance and easy capture by the reticuloendothelial and mononuclear phagocyte systems. (28, 29) One way to solve the aforementioned issues is the encapsulation of drugs in targeted drug delivery systems, usually surface-modified nanoparticles with hollow or porous interiors. Two FDA-approved examples for breast cancer treatment would be Doxil® and Caelyx®, both pegylated liposomal carriers of doxorubicin (Table 1).

Other promising works on new drug delivery systems (DDS) are published every year and involve not only polymers, lipids and proteins, but also polysaccharides, metals, ceramics, or a combination of two or more of these.(30-34)

Two other emerging cancer treatments are photothermal therapy and hyperthermia. The first consists in the conversion of photon energy into thermal energy inside the tumour, which results in a temperature increase and cell death by heat. The second therapy also proposes cell death by heat; however, this effect is achieved through the application of a magnetic field. Essentially, the energy which derives from relaxation after dipole alignment is converted into thermal energy, which then heats the particle surroundings and causes cell death. Most importantly, both techniques require the presence of an intermediate within the tumour microenvironment, preferably inside tumour cells, that is able to perform these energy conversions into heat. For photothermal therapy, gold nanoparticles have been presented as an option, while magnetic products such as superparamagnetic iron oxide nanoparticles (SPIONs) have been suggested for magnetic hyperthermia purposes.(35)

In short, targeted cancer therapies are an attractive branch of oncology, since they reduce most problems associated with these therapies. Future actions will still benefit from the combination of targeted drug delivery systems with surgery, contributing as an adjuvant treatment to the latter.

Table 1. Summarized table of some common drugs used for breast cancer treatment and new monoclonal antibodies (mAb) and nanoparticles for targeted therapy of breast carcinoma. HER2: human epidermal growth factor receptor 2; ER: estrogen receptor; TNBC: triple negative breast cancer.

Name (market name)	Description	Cancer	Ref.
Trastuzumab (Herceptin®)	HER2-targeting mAb	HER2+ breast cancer	(36)
Lapatinib (Tykerb®)	HER2 inhibitor	HER2+ breast cancer	(37)
Tamoxifen (Nolvadex®)	Aromatase inhibitor	ER+ breast cancer	(38)
Exemestane (Aromasin®)	Aromatase inhibitor	ER+ breast cancer	(39)
Paclitaxel (Abraxane®)	Nanoparticle albumin-paclitaxel	TNBC, lung, pancreatic cancer	(40, 41)
Doxorubicin (Doxil®)	Pegylated liposomal doxorubicin	TNBC, Kaposi's sarcoma, ovarian cancer	(42)
Doxorubicin (Caelyx®)	Pegylated liposomal doxorubicin	TNBC, ovarian cancer	(43, 44)

1.2. Nanotechnology

1.2.1. Basic definitions and impact in medicine

The definition of nanoparticle has been a subject of discussion in the scientific community for a long time. Most definitions include particles with less than 100nm in aerodynamic diameter(45, 46) while others also include materials with lengths between 1 and 100nm in two or three dimensions.(47) The definition of microparticles, on other hand, generally covers particles from 100nm to 100μm in diameter.(45) Irrespective of their differences, both have been of great utility in the development of new products and solutions across most areas of expertise.

Science has often taken advantage of the unique properties of nanoparticles for the creation of new products. Electronics, life sciences, environmental studies or textiles have much benefitted from the outstanding optical, magnetic, mechanical and chemical properties of systems that can be observed at the nanoscale. In medicine, nanoparticles have been used for many purposes, namely imaging contrast agents, drug and gene delivery systems, fluorescent probing, heat-induced treatments such as hyperthermia and photothermal therapy, molecule separation, and many others.(48)

1.2.2. Nanoparticles in MRI

As mentioned before, contrast agents in magnetic resonance imaging are of extreme importance for medical condition diagnostics.

Currently, paramagnetic gadolinium-based products are far more commonly used than iron oxide- or manganese-based contrast agents. However, many solutions for gadolinium are being investigated(49), given that numerous patients who suffered of acute or chronic renal insufficiency and to whom gadolinium-based contrast agents had been administered reported the occurrence of nephrogenic systemic fibrosis.(50-52) Substitutes in T1-weighted imaging would include biocompatible paramagnetic nanomaterials with high saturation magnetizations. Alternatively, some researchers shifted their attention towards T2-weighted imaging and iron-based products, generally with superparamagnetic properties.

Superparamagnetic iron oxide nanoparticles (SPIONs) were considered potential contrast agents in T2-weighted MRI due to their adequate physical properties and to the fact that the human body contains a considerably large iron pool, along with well-defined mechanisms to process and transport this element, unlike gadolinium.(53, 54) Numerous nano-systems with an iron oxide core have since been developed and are undergoing clinical trials, and are usually constituted by magnetite or maghemite.(49, 55) Both iron oxides become superparamagnetic at sizes below 20nm and ferrimagnetic above 20nm.(56)

It should be emphasized that, for T2-weighted imaging, iron products should not just be superparamagnetic but also have high saturation magnetization values. Briefly, most iron products do show high magnetization values but are ferromagnetic, which means that some magnetization remains after applying sequential magnetic pulses. Now, naturally, remanent magnetization in a clinical context is best avoided, so iron-based products with no remanent magnetization were considered the ideal solution. This includes the abovementioned SPIONs, which report zero remanent magnetization owing to their superparamagnetism.

Some concerns, however, are still raised in regard to the biocompatibility of iron materials, and so iron-doped hydroxyapatite with superparamagnetic characteristics was suggested as a better alternative by Tampieri, Gloria, Laranjeira, and respective teams.(57-59)

1.2.3. Nanoparticles in drug delivery

1.2.3.1. Stimuli-responsive drug delivery

A substantial number of drugs have reported poor pharmacokinetic behaviour when administered freely, namely fast renal clearance and low circulation half-life. This increases the need for additional and more frequent dose administrations to patients. Sustained release of the drug, either occurring spontaneously or following the induction of a stimulus, would be an interesting solution to this problem. This can be achieved by incorporating the drug into "smart" nanocarrier systems that can respond to these triggers, taking advantage of the remarkable physicochemical properties of some materials. In medicine, this would be a potential solution not just for cancer treatments but also for other medical purposes - menopausal therapy, fungal infections, multiple sclerosis, hepatitis B and C, or rheumatoid arthritis.(49)

Drugs can be incorporated into the transport system in a wide variety of ways, depending on material and drug chemistry. With increasing advances in particle synthesis and chemistry, more creative ways of performing the combination drug-carrier tend to appear. As of 2016, eight anticancer drug delivery products based either in protein-drug conjugates, or lipid- or polymer-drug combinations, were available in the market, and several other are under clinical trials.(49)

Stimuli for drug release could be internally or externally applied. External stimuli include magnetic field, electric field, ultrasound, or light, usually UV or near-infrared (NIR), while internal stimuli cover pH, temperature, or enzymatic action (Table 2).(60)

The application of an external magnetic field is mostly used in combination with magnetic or partially magnetic nano-systems. As explained before, some magnetic nanoparticles in suspension are able to convert electromagnetic energy into thermal energy through Brownian and/or Néel relaxation(61) to produce hyperthermia effects. Given this asset, some researchers devised the addition of one other functionality - drug delivery - either through conjugation of the drug to the magnetic nanoparticles or the combination of magnetic nanoparticles with hollow or porous nanocarriers. Some nanocarriers may be sensitive to magnetic fields and consequently heat, rupturing or shrinking its structure and releasing the drug. Rupturing materials include, for instance, liposomes or peptide structures (Table 2), and shrinking materials include the well-known thermo-responsive polymer poly(N-isopropylacrylamide) (PNIPAM). Magnetic

field-responsive drug release systems count many advantages, along with another functionality - physically displacing and controlling cell positions *in vivo*. Naturally, though, the requirement of strong magnets and specialized technicians is a limitation of such an option.(60)

A material is considered piezoelectric when the exertion of a mechanical force translates into an electrical polarization, and vice-versa. Most published works on piezoelectric structures for drug delivery propose the development of micropumps for micro-electrical mechanical systems (MEMS) (Table 2), but another interesting piezoelectric material is synthetic hydroxyapatite. Hydroxyapatite (HAP) was thought to be centrosymmetric until Haverty proposed that polar, hexagonal nanoHAP could be non-centrosymmetric.(62) This changed some views on the physicochemical properties of bone, namely pyro- and piezoelectricity, which were formerly attributed to collagen and were now also attributed to the ceramic.(63) The heating of pyroelectric nanoHAP could render it interesting for thermally-triggered drug release purposes and the mechanical stress to which it is subjected may also disrupt the electrical equilibrium inside the cells. Nevertheless, to this date there are no published works on piezoelectric or the pyroelectric properties of hydroxyapatite in controlled drug release(64), only for tissue engineering(64, 65) and biological sensors.(66-69)

Other types of stimuli include electric fields, ultrasound, and light. Regarding electric fields, generally, by employing polyelectrolytes of either natural or synthetic origins, an electric field-responsive system may be easily built. The idea for this type of trigger is relatively new, and therefore needs more testing.(60) Ultrasounds are able to penetrate tissue and reach considerable depths with spatial precision and without harm - one of the main reasons why it has also been suggested as a potential trigger for drug release. Temporary pores in the matrix of adequate materials (low frequency ultrasounds) or complete disruption (high frequency ultrasounds), along with enhanced cell permeability, would account for the drug release and uptake processes (Table 2). Similar to ultrasounds, light may also be applied as an external stimulus.

Ultraviolet (UV) light, for instance, has enough energy to break a considerable number of labile chemical bonds but is mutagenic. Near-infrared light (NIR) is then presented as a safer alternative with transparency to blood and tissue, good spatial precision and biologically-friendly wavelength ranges (650-950 nm). NIR photon energy may also be converted into heat and may cause hyperthermia or, in the case of gold nanoparticles, photothermal effect due to surface plasmon resonance.(70)

Temperature is a versatile trigger for drug release, as it may derive from external or internal action. As seen before, the energy resulting from the application of magnetic fields, electric fields or light can easily be converted to thermal energy. Concerning internal mechanisms, inflammation and fever are the main processes associated with

temperature increase, along with the tumour milieu, which is generally 2-3°C warmer than other tissues due to increased metabolic activity.(71)

Table 2. Summarized table of external and internal stimuli for "smart" drug release. DOX: doxorubicin, NIR: near infrared (light), PTX: paclitaxel

Stimulus	Method of action	Examples	References
Magnetic field	Rupture, induction of physical changes in the carrier structure	Magnetoliposome loaded with DOX; Poly(allylamine)-magnetite loaded with DOX	(72, 73)
Electric field	Size change, folding, erosion, pressure	Hyaluronic acid carriers; micropumps	(74) (75-77)
Ultrasound	Pore induction, structure disruption	Polylactide-based micelles loaded with DOX	(78)
Light	Pore induction, structure disruption	Copolymer micelles loaded with PTX	(79)
Temperature	Size change; rupture	Liposomes and copolymers loaded with chemotherapy drugs	(80-82)
pH	Size change	Copolymers loaded with chemotherapy drugs	(32, 80)
Enzymes	Rupture	Nucleic acid nanocapsules	(83)

In the design of this kind of nanosystems, it is important to know the concept of lower critical solution temperature (LCST), the temperature at which the material suffers a phase transition from a more hydrophilic to a more hydrophobic state, and volume phase transition temperature (VPTT), which corresponds to the temperature at which the polymer dramatically changes its volume. The VPTT generally coincides with the LCST. Below the LCST, hydrophilic forces prevail and the polymer chains will be extended, resulting in a swollen gel; above the LCST, hydrophobic forces will overtake hydrophilic ones and as a result the hydrogel will rapidly contract to a globular form, releasing all of its contents into the aqueous medium, e.g. drugs and molecules.

Most temperature-triggered nano-systems can be hydrogels, liposomes, micelles, and micro- or nanogels.(60) They can be made from thermosensitive materials such as poly(N-isopropylacrylamide) (PNIPAM, LCST of 32°C); poly(vinylpyrrolidone) (PVP) and derivatives; or even some lipids whose melting temperature lies in a biologically relevant range (38-45°C) (Table 2).

The advantages of using this kind of stimulus are the easy procedure for preparation and scale-up of most thermosensitive carrier systems. Disadvantages include the optimization of particle size for clinical administration, which generally requires a size smaller than 200 nm(84), and the use of materials which have not yet been approved by the FDA, such as PNIPAM.

Changes in pH are one other trigger used in for controlled drug release. There are distinct pH values for healthy and affected tissues, organs, and cellular compartments. The tumour extracellular environment is slightly acidic (60, 85), arterial pH is at ~7.4 (86), intracellular fluid of tumour cells is at approximately pH 6.5-7.2 and endosomes are at pH 5-5.5 (85, 87, 88). Materials responsive to pH are, for example, poly(methacrylic) or poly(acrylic) acid (PMAA and PAA) and their many derivatives, including the largely commercialized Eudragit®.(89) Limitations of this technique rely on the eventual passage of the nano-system through compartments which have the desired pH but in which release is not yet desirable.

Lastly, enzymes are especially designed to cleave certain chemical bonds, an excellent mode of action for selective drug release. The use of enzymes for drug release is advantageous because it is free of toxic materials and relies on the action of well-defined biological mechanisms.

1.2.3.2. Calcium phosphates

Calcium phosphates are one of the most used ceramics in bone tissue engineering, in particular hydroxyapatite and tricalcium phosphates. These materials were introduced as alternatives to allografts, xenografts or autografts, or bone substitutes such as titanium alloys, stainless steel, or poly(methyl methacrylate) (PMMA) due to their excellent thermodynamic stability at physiological pH and biosimilarity with the mineral

component of bone.(90) Possible drawbacks of calcium phosphates result from its brittleness and low tensile strength (91); fortunately, the impact of such properties does not apply so much to nanomaterials. Its use has been widened to include biomedical and non-biomedical purposes such as chemical catalysis, radioactive waste disposal (92), dentistry and gene and drug delivery.(93, 94)

Tricalcium phosphates (TCP) are characterized by the composition $Ca_3(PO_4)_2$ and usually have three polymorphs: α-, ß- and α'-TCP, with α- and ß-TCP being the most common types. Both are biocompatible, with α-TCP being more biodegradable, and both are more easily degradable than hydroxyapatite (HAP). Notably, α-TCP is often converted in HAP. The α- form is characteristic of higher temperatures, while the ß- is commonly found at room temperature. Overall, TCP is FDA-approved and vastly commercialized worldwide. For drug delivery purposes, TCP has been often studied for sustained release of antibiotics or proteins, usually in combination with an alginate matrix.(95-98)

Hydroxyapatite (HAP) is represented by $Ca_{10}(PO_4)_6(OH)_2$ and may be identified by a calcium-phosphorus (Ca/P) ratio of 1.67. It is one of the most stable calcium phosphates in biological environments, it is characterized by a hexagonal structure and has proven to be pyro- and piezoelectric at the nanoscale as long as it is electrically polar. Quite a few methods for the synthesis of nanoHAP have been proposed in the past fifty years, some of which are wet chemical precipitation, hydrothermal synthesis, sol-gel, or microwave synthesis.(99) Of these, the most frequent choice is wet chemical precipitation, due to its pure yield, simplicity, use of environmentally-friendly aqueous solvents, possibility of scale-up and cost-effectiveness.(93) One possible protocol for the synthesis of nanoHAP entails the slow addition of orthophosphoric acid (H_3PO_4) to a calcium hydroxide solution, with varying temperatures and pH. (59, 100, 101) The chemical equation for such reaction is presented in Eq.1.

$$10Ca(OH)_2 + 6H_3PO_4 \rightarrow Ca_{10}(PO_4)_6(OH)_2 + 18H_2O \qquad (1)$$
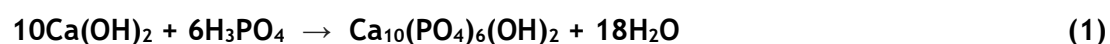
In this reaction, alkalinity is important to ensure that the final product is pure hydroxyapatite. Nevertheless, small phases of tricalcium phosphate (TCP) may be found in the final hydroxyapatite product. Such phases are not problematic since they normally represent less than 1% of the total structure.(101, 102) Incorporation of other ions in the lattice by exchange with Ca^{2+} may also occur under certain conditions, which constitutes a potentially useful phenomenon.(59) Ashokan and team developed europium- and gadolinium-doped hydroxyapatite nanoparticles by adding solutions of the respective salts in simultaneous with orthophosphoric acid without the addition of surfactants (103), while Laranjeira, Moço and team proved that magnetic nanohydroxyapatite could be produced by doping HAP with iron(II), iron(III), gadolinium and cobalt.(59) Despite the

biocompatibility of this ceramic and low hemolysis, slight thrombogenicity for iron-doped nanoHAP was observed. (59, 104) Lastly, Tampieri, Gloria and respective teams proved that iron-doped nanoHAP could exhibit superparamagnetism, an excellent indicator of the potential of this doped ceramic.

1.2.3.3. Thermo-responsive polymers

"Smart" polymers, i.e., polymers that respond to stimuli, are emerging as an extremely promising category of materials for biomedical engineering. As described before, the most common stimuli for polymers are temperature and pH. While many polymers can be pH-responsive, thermal responsivity for biomaterial purposes is mostly represented by one polymer: PNIPAM. Indeed, its LCST of 32°C is close to the regular human body temperature, and can be easily adjusted to a higher critical temperature when copolymerized with hydrophilic monomers.(88, 105) Adding to its versatility, PNIPAM-based nanocarriers bring all the advantages associated with temperature-triggered drug delivery systems; however, this material is yet to be approved by the FDA for biomedical applications.

PNIPAM results from the polymerization of N-(isopropylacrylamide), a relatively neutral monomer. While polymer syntheses can be performed through atom transfer radical polymerization (ATRP) or reverse addition-fragmentation chain-transfer polymerization (RAFT), the overall preferred protocol is free radical polymerization. Free radical polymerization (FRP) is simple, versatile, and consists in a polymer chain growth induced by the action of a radical initiator and helped by the presence of a crosslinker. The FRP of NIPAM, for instance, commonly employs N,N-methylenebisacrylamide as the crosslinker. As for the radical initiator, the choices are endless - photoactivated azo-compounds, benzoyl peroxide or persulfates like potassium persulfate or ammonium persulfate (APS). Free radical copolymerization can be performed not just with acrylamides but also with acrylates and methacrylates, which may add functionalities to the thermally responsive PNIPAM. A representation of free radical copolymerization of NIPAM with two monomers relevant for this work is shown in Fig.2. The monomers are 2-(dimethyl aminoethyl) methacrylate (DMAEMA) and a single-methacrylate modified poly(ethylene glycol), poly(ethylene glycol) methacrylate (PEGMA).

Some methacrylates have already been approved by the FDA for certain applications or are currently undergoing clinical trials – poly(methyl methacrylate) (PMMA) has proven important as a bone void filler in spine surgery, while poly(2-hydroxyethyl methacrylate) (PHEMA) is a known component of contact lenses.

DMAEMA is a pH-sensitive, water soluble, tertiary amine methacrylate monomer. The combination of small quantities of DMAEMA with NIPAM has been attempted before in

the design of stimuli-responsive drug delivery systems.(81, 106, 107) In these works, despite the pKa of DMAEMA being 7.5(108), the main purpose in using this monomer was the tuning of the final core-shell microgel LCST to values closer to 40°C. Its pH-responsivity was shown to be considerably overrun by the thermo-responsivity of NIPAM, due to the use of small amounts of DMAEMA during synthesis.
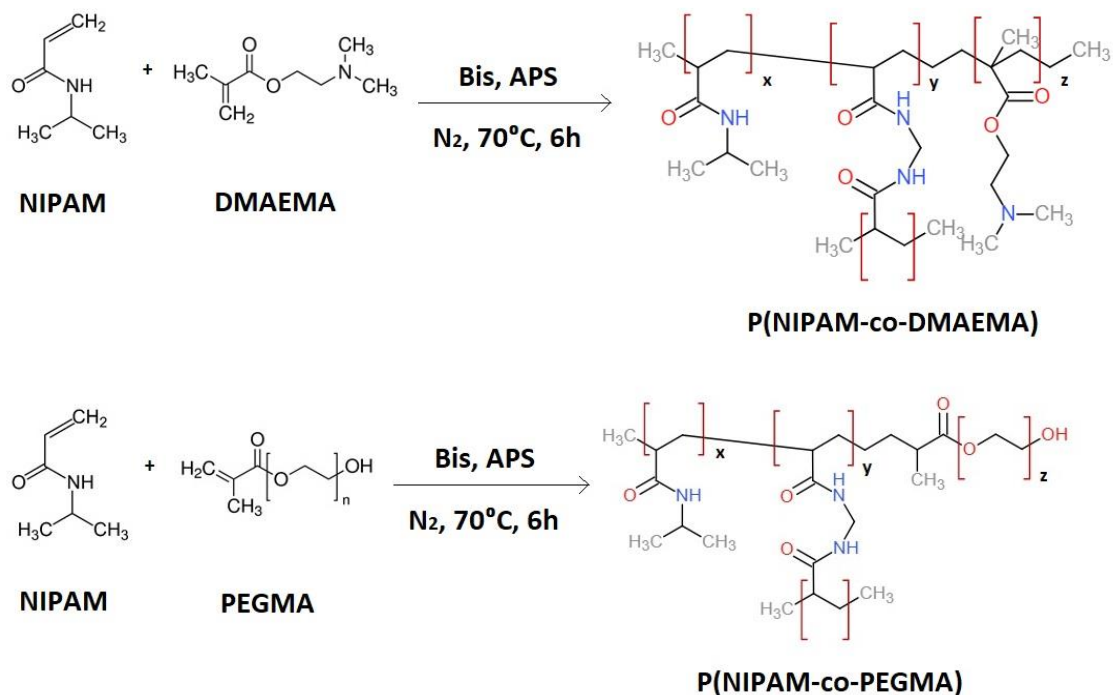
Figure 2. Schematic representation of a free radical copolymerization of NIPAM with 2-(dimethylaminoethyl) methacrylate (DMAEMA) *(top image)* or with poly(ethylene glycol) methacrylate (PEGMA) *(bottom image)*, with N,N-methylenebisacrylamide (Bis) as a crosslinker (y portions) and ammonium persulfate (APS) as an initiator. These syntheses were employed in the present work.

A wide spectrum of reagents with lower pKa could be chosen instead of DMAEMA for a better controlled release. However, DMAEMA possesses one very promising property – excellent gene transfection rates.(108) While it is not vastly explored in the scope of this work, the potential for gene therapy and delivery is immense. In short, not only does DMAEMA provide good LCST tuning when copolymerized with PNIPAM, it also has a remarkable potential in a field of broad and current interest.

Along with the development of copolymer microgels of P(NIPAM-DMAEMA) for chemotherapeutic drug delivery by the team of Prof. Davaran(81, 106, 107), Loh and team built a cationic co-delivery system of both drug and DNA, formed by a copolymer of DMAEMA and propylene glycol methacrylate (PGMA).(109) More recently, the team of

Prof. Wung designed chemotherapy drug and gene codelivery systems involving a copolymer of DMAEMA and hydroxybutyrate for liver cancer therapy.(110, 111)

Poly(ethylene glycol) methacrylate (PEGMA) results from one of the many possible modifications of poly(ethylene glycol) (PEG). It consists of a polymeric chain of ethylene glycol of variable length, modified on one end with a methacrylate group whilst maintaining its other OH- termination. Jones and Lyon first attempted to produce and characterize copolymers of NIPAM and PEGMA(112), and more recently Knop and team developed PEGMA-containing brush-like shells for doxorubicin drug delivery.(113) Many other studies involving PEGMA are being developed, but application of PEGMA in microgels is still relatively unexplored.

The potential of PEG is widely known. It is an FDA-approved hydrophilic polymer which has been applied to many different products, not just in medicine but also in cosmetics and pharmaceuticals.(114) In drug delivery systems design, it is used as a coating or as an intrinsic part of the nanocarrier formulation, to stabilize suspensions or increase their blood circulation half-life. By having high affinity towards albumin, an abundant protein in the bloodstream, pegylated nano-systems tend to be masked after albumin adsorption, and ultimately protected against the detection of immune system-related proteins, e.g. opsonins. Owing to its outstanding properties in biological media, research groups and companies have dedicated to modifying PEG terminations in order to better suit a large number of applications, of which PEGMA is an example. Covalently linking PEG to a polymeric matrix ensures that this hydrophilic molecule is securely incorporated in the material and maintains its beneficial properties.

1.2.4. Nanoparticle Pharmacokinetics

Pharmacokinetic analysis is of paramount importance when designing, developing and characterizing a nanoscale system for biomedical and pharmaceutical applications. Pharmacokinetics comprises five main categories: administration routes, (bio)distribution, metabolism, excretion and toxicity – a set of parameters commonly known in pharmaceutical sciences as ADMET evaluation.

Firstly, there are numerous administration routes. Oral administration is frequently considered the best option due to its simplicity, slow release and clear preference among patients – nevertheless, it must be subject of the effect of first-pass through the enterohepatic system, thus affecting functionality and, in some cases, drug bioavailability.(115) Adding to this, since the gastrointestinal tract has widely varying pH values, related routes are not adequate for pH-sensitive systems. Intravenous administration often appears as the ideal alternative for stimulus-responsive drug delivery systems, especially for cancer therapy, owing to high bioavailability, fast

response, and easy reach to tumour-affected areas as a result of the EPR effect. Disadvantages include the need for sterilization and skilled medical personnel.

After administration of the nano-system, biodistribution takes place throughout the organism. During blood circulation, hydrophilic structures tend to bind an endless number of serum proteins before accumulating in the organs.(116) As seen in the case of PEG, albumin rapidly masks the pegylated material, protecting it from the adsorption of opsonins that, when bound to the surface of foreign objects, can trigger the object uptake by cells of the reticuloendothelial system (RES), especially macrophages. Opsonin detection reduces the mean resident life in circulation of the object and increases their clearance, excreting a considerable number of nanoparticles before their function is fulfilled.

Most metabolic processing occurs after cell uptake of the particles, mainly in organs such as the liver, spleen, and kidney. Such uptake will depend on factors such as object size and shape – particles with diameter of 10-12nm are not immediately eliminated and do not get easily retained in organs, and more elongated particles tend to penetrate better than spheres.(117) The most accepted sequence for metabolic actions consists in i) cell influx mediated by proteins of the solute-linked carrier superfamily (118); ii) redox reactions and hydrolysis performed by cytochromes (e.g. cytochrome P450); iii) conjugation reactions with polar groups for easier excretion; and iv) cell efflux, usually mediated by p-glycoprotein.(119)

Subsequently, excretion occurs, mainly at renal level but also through perspiration or exhalation. Size takes an important role in this biological process - after administration, immediate renal clearance is observed in particles with less that 5.5 nm.(120) Larger particles, in the range of 5-200 nm, tend to be captured by Kupffer cells of the liver and suffer hepatic clearance, especially at sizes closer to 200 nm. Particles of 300 nm tend to get retained in the spleen by red pulp macrophages and then suffer splenic clearance. Administration of nanostructures larger than 300 nm is advised against, due to the risk of emboly.(121) An additional problem related to clearance, or lack thereof, is bioaccumulation. Inorganic particles such as iron oxide- or gadolinium-based are resistant to lysosomal processing, and thus tend to accumulate in the liver, spleen or the kidneys(122), possibly giving rise to serious conditions such as nephrogenic systemic fibrosis.

Lastly, still related to bioaccumulation, there is toxicity. Toxicity is defined as the ability of damaging or causing adverse effects in the organism, and depends on factors such as size, shape or surface charge of the particle.(123) As described before, systems larger than 300 nm are likely to agglomerate and occlude capillary vessels or cause emboly. Regarding shape, higher aspect ratio particles usually translate into a higher uptake, as explained before, also contributing to further toxicity if the material is not sufficiently biocompatible. Concerning charge, nano-systems with charged surfaces are more easily uptaken than neutral charge systems, especially if they are cationic - anionic particles tend to be repelled by the exterior negative charge of cellular membranes. It

is known that anionic particles are less toxic than their cationic counterparts, possibly due to their interaction with some enzymes.(124) Within cationic factors, differences in cytotoxicity can be attributed to the hydrophilic group form. For instance, quaternary amines are more toxic than tertiary amines, present in materials such as DMAEMA.(124) In addition to bioaccumulation of inorganic particles, these can also be responsible for an increase in reactive oxygen species (ROS) caused by redox imbalances in the mitochondria.

Clinical failure in polymeric particle testing has been generally caused by the lack of specific targeting to the desired sites within the human body. Surface modification for targeting and development of release-upon-trigger drug delivery systems would largely improve polymeric nanocarrier success in clinics.(124, 125) A careful analysis of these five gold parameters of pharmacokinetics is thus essential to a correct nano-system design.

1.3. Aim

In recent years, the condensation of targeted therapy and diagnostics in one single system gave rise to the new concept of theranostics. Working towards patient-oriented solutions, it has risen as a contributor to the development of personalized medicine. Advances in materials science have unveiled great potential for biomedical applications in materials otherwise never thought to be used in medicine. In fact, with resort to biological, physical and chemical adaptations, biomedical and biopharmaceutical research have offered rather creative solutions for current shortcomings in injury treatment, disease therapy, and general drug delivery.

The purpose of the present work was to develop a cancer therapy- and diagnostic-oriented nanocomposite system for controlled drug delivery and MRI contrasting (Table 3). Iron(III)-doped hydroxyapatite (FeHAP) nanoparticles were produced according to an adapted protocol from the work of Laranjeira and Moço(59) and characterized in terms of size, shape, surface charge, chemical profile, crystallinity and magnetic properties. The iron(III) ion substitution percentage of calcium ions was set at 10%. Next, polymeric microgels composed by a thermoresponsive P(NIPAM-co-DMAEMA) core and a P(NIPAM-co-PEGMA) shell were synthesized, optimized and characterized in terms of size, shape, thermal response, and chemical profile. The encapsulation of the ceramic particles in the microgels was attempted, along with the encapsulation of the poorly water-soluble drug doxorubicin (DOX). Drug loading onto the microgels was analyzed along with microgel effects in the metabolic activity of human gingival fibroblasts (HGF).
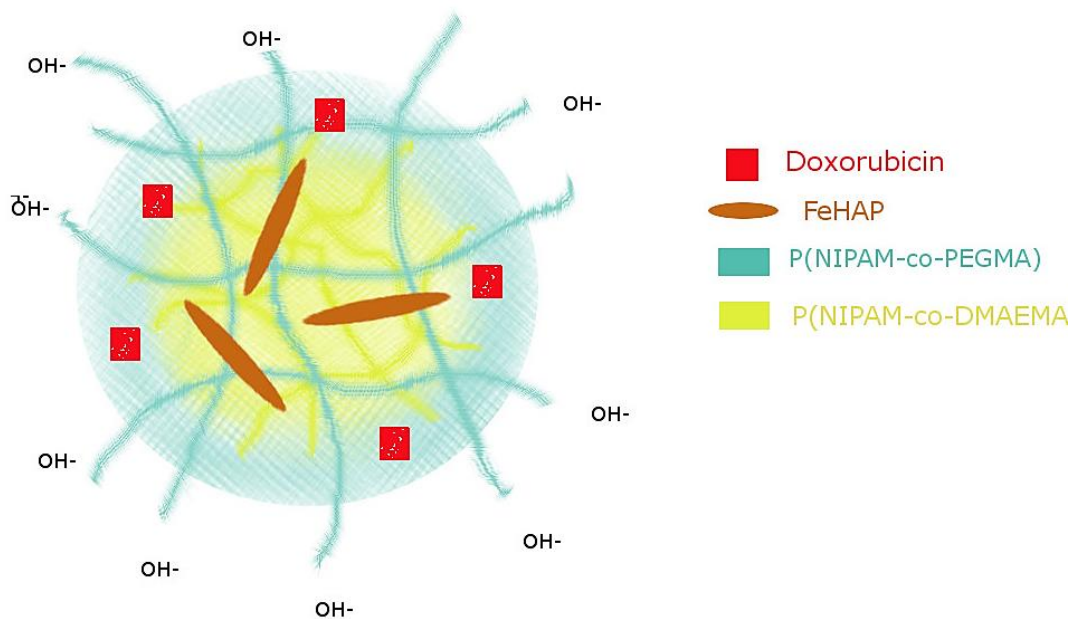
Figure 3. Schematic representation of the nanosystem developed in the present work. Both drug and ceramic are encapsulated inside the core-shell microgel.

Table 3. Summary of the individual components of the nanoscale drug delivery system proposed in this work, desired characteristics and main purposes.

System Component	Core-shell microgel	Iron(III)-doped hydroxyapatite	Doxorubicin
Characteristics	Core: P(NIPAM-co-DMAEMA) Shell: P(NIPAM-co-PEGMA) LCST: 38-39ºC Size: <250nm (25ºC) Reduced protein adsorption	Iron/calcium substitution: 10% Ca/P ratio: 1.67 Size: <100nm Shape: elongated Ferro-, para- or superparamagnetic	Hydrophobic DNA-damaging
Main Purpose	Transport; Protection of ceramics from degradation; Reduction of drug clearance;	Cancer cell apoptosis; MRI contrasting	Cancer cell death

The fact that tumours are generally at higher temperatures than non-affected tissue is a premise for internally-triggered drug release. As such, nanocarriers with a VPTT set between 38 and 39ºC would release most of its load above these temperatures, mostly inside the tumour milieu. Also, due to the EPR effect, these particles would naturally tend to accumulate in such regions.

Iron-doped HAP nanoparticles are shown as a less cytotoxic alternative to currently employed contrast agents, all while attempting to retain their magnetic properties. Additionally, when inside the endosome or lysosome, calcium degradation contributes to the disruption of membrane homeostasis and may possibly induce apoptosis, while iron liberation may result in higher ROS production. In short, both are toxicity-inducing agents when degraded within the cell.

If iron-doped HAP is proven superparamagnetic, it may be employed as a contrast agent for T2-weighted MRI imaging. Encapsulated in a microgel matrix, this ceramic would be further protected from degradation in the bloodstream and would be delivered to the target cancerous tissue.

Parallel advances in nanomedicine, molecular biology, and clinical medicine will hopefully enable a fast mapping of the most affected organs for the design of unique treatments with the highest efficiency rates and the least side effects. In this way, the high versatility of drug nanocarriers is expected to constitute a major asset for the yet-developing concept of personalized medicine.

(page intentionally left blank)

Chapter II

Experimental Procedures

2.1. Materials

For the synthesis of ceramic nanoparticles, iron(III) nitrate nonahydrate (98+%), calcium hydroxide (98%), phosphoric acid (85 wt% solution in water) and ammonium hydroxide (25% solution in water) were purchased from Acros Organics, USA.

For the synthesis of polymeric nanoparticles, N-(isopropylacrylamide) (NIPAM, 97%), N,N'-methylenebis(acrylamide) (Bis, 99%), ammonium persulfate (APS, >98 %), 2-(dimethylamino)ethyl methacrylate (DMAEMA) and poly(ethylene glycol) methacrylate (PEGMA, average Mn 500) were purchased from Sigma-Aldrich, Germany.

Sodium citrate tribasic dihydrate (NaCit, ≥99.0%) sodium dodecyl sulfate solution (20% in water) and doxorubicin hydrochloride (DOX HCl, 98.0-102.0%) were also purchased from Sigma-Aldrich (Germany).

Primary cultures of human gingival fibroblasts were purchased from Sciencell (USA) and cultured in 96-well cell culture plates with α-MEM medium (Sigma, Germany) containing fetal bovine serum (FBS, Gibco, USA), a penicillin/streptomycin solution (Biowest, France) and fungizone (Capricorn Scientific, Germany). Resazurin for cell metabolic activity assays was purchased from Sigma-Aldrich, Germany.

All chemicals were used without previous purification and all syntheses were performed using ultrapure water of resistivity 18.2MΩ.

2.2. Synthesis of Ceramic Nanoparticles

2.2.1. Synthesis of hydroxyapatite nanoparticles

Hydroxyapatite (HAP) and iron(III)-doped hydroxyapatite (FeHAP) nanoparticles were synthesized through a wet precipitation method.(59, 103) Briefly, for pure hydroxyapatite nanoparticles, 40mL of a solution of calcium hydroxide 0.5M were heated at 95ºC in an oil bath under vigorous magnetic stirring. Then, 40mL of a solution of 0.3M orthophosphoric acid were then added at a rate of 0.500mL/minute using a Gilson MiniPuls3 peristaltic pump (Gilson, USA). The pH of the reaction was kept above 9.5 throughout the whole experiment by adding ammonium hydroxide (25% in water) as needed. After the orthophosphoric acid addition, the reaction was maintained at 95ºC for 2 more hours. The mixture was cooled down and centrifuged thrice for 3 minutes at 2500rpm (1251g) in an Eppendorf Centrifuge 5810R (Eppendorf, Germany). The supernatant was removed, the nanoparticles were redispersed in deionized water and the resulting slurry was spread on a Petri dish and left to dry overnight in a flow hood. The dried particles were then ground with pestle and mortar, weighted, and stored in a desiccator.

Furthermore, for some characterization techniques, a small portion of the resulting powder was sintered at 1000ºC for one hour, with a heating rate of 5ºC/min and natural cooling until room temperature. The resulting grains were also stored in a desiccator.

2.2.2. Synthesis of iron(III)-doped hydroxyapatite nanoparticles

The synthesis of iron(III)-doped hydroxyapatite nanoparticles with a Fe^{3+}/Ca^{2+} atomic substitution of 10% involved the simultaneous addition of 20mL of orthophosphoric acid 0.6M and 20mL of an iron(III) nitrate nonahydrate solution 0.1M to the calcium hydroxide 0.5M solution at the same rate (0.500mL/min). The remaining reaction, washing, drying and storage process details were the same as the protocol for the synthesis of pure hydroxyapatite nanoparticles, above described. The sintering process afterwards was also similar to the above described, with a heating rate of 5ºC/min and one-hour dwelling plateau at 1000ºC, followed by cooling down to room temperature. All samples were stored in a desiccator.

2.3. Characterization of Ceramic Nanoparticles

2.3.1. Size and surface charge

Hydrodynamic diameter measurements were done through dynamic light scattering (DLS) and surface charge measurements were obtained through zeta potential analysis. Both were performed with a Malvern ZetaSizer Nano ZS (Malvern, UK) comprising a He-Ne 633nm wavelength laser with a scattering angle of 173º. The measurements were performed at i3s, Porto, Portugal.

Dynamic light scattering is a technique through which the hydrodynamic radii of nanoparticles or proteins in suspension can be estimated. It is based on the study of particle diffusion through Brownian motion, which can then be related to hydrodynamic size through the Stokes-Einstein equation (Eq. 2).

$$D = kT/6\pi\eta R$$

(2)

D represents the diffusion coefficient of the particles, κ the Boltzmann constant, T the temperature, η the shear viscosity of the solvent and R the hydrodynamic radius. In dynamic light scattering, a monochromatic laser is passed through the sample and, due to the random motion of the particles, the light is scattered differently depending on their hydrodynamic size. This light is then detected and analysed to produce a final particle size distribution.

Zeta potential measurements, on other hand, give information on the surface charge of a colloidal suspension. By applying an electric field through the sample, charged particles migrate depending on their own properties. Their electrophoretic mobility is then determined through light scattering using the same principle as the hydrodynamic size determination and translated into a surface charge distribution.

The preparation of the samples was made by dispersing the ground non-sintered ceramic powders in an aqueous solution of 10mg/mL sodium citrate for a final particle concentration of 10mg/mL. Sodium citrate was used as a dispersant for a more accurate measurement of the hydrodynamic diameter of individual particles. The suspension was then sonicated in an ultrasonic bath (Sonorex Digitec, Bandelin, Germany) for 1 hour and diluted 20 times in ultrapure water for analysis. Three size and zeta potential measurements were made per sample, at 25ºC.

2.3.2. Chemical profile

The chemical profile of the nanoparticles was performed by Raman spectroscopy and Fourier Transform Infrared Spectroscopy (FTIR) under transmittance mode.

Raman spectroscopy was performed in a T64000 Jobin-Yvon spectrometer (Horiba, Japan) with a He-Ne laser of 514.5nm wavelength and a spectral resolution of 0.15 cm-1. FTIR was performed in a Perkin-Elmer 2000 (Perkin-Elmer, USA) with a $4cm^{-1}$ spectral resolution and 32 scans per sample. Raman measurements were performed at the IFIMUP-IN, University of Porto, while FTIR was performed at i3s, Porto.

Raman spectroscopy is a technique that provides information on the chemical bonds that exist in a sample. It is based on the principle that, when irradiating a sample with a monochromatic laser, a small part of the electrons does not return to the same initial energy state, emitting or absorbing more energy. The resulting scattered energy – Raman scattering - is a fingerprint of each molecule, and can be detected and processed into a Raman spectrum for easier identification of the molecules present in the sample.

Similarly, FTIR also provides information on the functional groups and chemical bonds that exist in a sample. It is based on the principle that, when irradiating a sample with a spectrum of infrared light, each molecular bond will absorb more energy at specific wavelengths and consequently less light will reach the detector. After the application of a Fourier transform to this raw data, the final transmittance or absorbance spectrum shows sudden drops or sudden peaks at the specific wavelengths at which light was absorbed, respectively. Each drop or peak is then compared with a database for identification of the chemical profile of the sample.

For Raman spectroscopy, a small amount of non-sintered ceramic powders (<1mm) and sintered ceramic powders (>1mm) were placed on a glass substrate. Several grain regions were analysed with different optimization parameters, namely regarding laser attenuation and acquisition time.

For FTIR, approximately 2mg of the ceramic powders were ground, mixed with 200mg of potassium bromide (KBr) pellet and compressed with a hydraulic press (Specac, UK). Pellets were produced in a low humidity environment to improve sample quality.

2.3.3. Crystallinity

Crystalline phase characterization was performed by X-ray diffraction (XRD) in a Rigaku SmartLab® operating at 9kW power (40kV and 200mA) and a copper source of wavelength 1.54Å. The diffractograms were represented as the diffracted particle intensity *versus* 2θ and a comparative analysis was made with base on the JCPDS database of the International Centre for Diffraction Data and Rigaku software PDXL. The

analyses were performed by Dr. Ana Pires at IFIMUP-IN, University of Porto. The samples were analysed in their dry powder form.

XRD is a technique used to infer about the crystal structure of a sample. The analysis consists in directing monochromatic X-rays at different angles towards a powder sample, which will diffract the rays differently and produce a unique diffraction pattern. Briefly, at the atomic level, when atoms diffract beams at the same angle of diffraction with the same phase, adding themselves constructively, the detector processes this signal into an intensity peak. This phenomenon is described by Bragg's Law (Eq.3).

$$n\lambda = 2d\sin\theta$$

(3)

In this equation, *n* is an integer representing multiples of the wavelength, λ is the incident X-ray wavelength, *d* is the interplanar distance (between two atomic planes) and θ the diffraction angle. The final processed diffractogram is composed of single peaks at specific angles, generally corresponding to the lattice planes of the crystals.

2.3.4. Morphology

Nanoparticles size and shape were assessed by transmission electron microscopy (TEM) in a JEOL JEM-1400 Electron Microscope (JEOL Ltd., Tokyo, Japan), operating at an accelerating voltage of 120kV. Images were recorded using a CCD digital camera Orious 1100W (Tokyo, Japan). This analysis was performed at i3S, Porto. TEM images were analysed with ImageJ® software (University of Wisconsin, USA).

Transmission electron microscopy is a technique used to observe nanoscale structures at a two-dimensional scale. By directing accelerated, condensed electrons towards a sample, scattering occurs. These scattered electrons are then focused and projected onto an appropriate phosphorescent plate to produce a high-resolution image.

The samples were prepared by dispersing the ceramic powders in an aqueous solution of sodium citrate 10mg/mL and sonicating, as described before, and then diluting approximately 100µL of sonicated sample in 1mL ultrapure water. A 10µL drop was then loaded onto a Formvar/carbon film-coated nickel mesh grids (Electron Microscopy Sciences, USA) for 30 seconds, after which excess liquid was removed with filter paper.

2.3.5. Magnetic properties

The magnetization of the ceramic iron-doped nanoparticles was studied in a Physical Property Measurement System at a temperature of 300K, at a magnetic field range from -30kOe to 30kOe. The measurement was performed at the Imperial College London by

Dr. Lesley Cohen and Dr. André Pereira. The ceramic samples were analysed in their dry form.

Under a varying magnetic field, the study of the magnetization of a sample can provide information about its magnetic behaviour and other possibly relevant parameters such as saturation or remanent magnetization values.

2.4. Synthesis of Polymeric Microgels

2.4.1. Synthesis of P(NIPAM) microgels

Poly(N-Isopropylacrylamide) was synthesized via free radical polymerization according to Schild(126). Briefly, 0.700g of N-Isopropylacrylamide (NIPAM), 0.025g of N,N'-methylenebisacrylamide (Bis) and 0.100mL of sodium dodecyl sulfate 20% solution (SDS) were mixed and dissolved in 40mL ultrapure water in a 250mL three-neck round bottom flask. This solution was then heated at 70ºC in a water bath and then purged with nitrogen for 20 minutes while stirring at 300rpm on a magnetic plate. In parallel, 0.032g of ammonium persulfate (APS) were dissolved in 10mL ultrapure water and equally purged with nitrogen for 15 minutes while stirring at 200rpm on a magnetic plate. After both purges, the APS solution was slowly added to the main reaction. The final reaction would have a monomer (NIPAM) concentration of 124mM, crosslinker (Bis) concentration of 3.4mM, initiator concentration of 2.7mM and a stabilizer concentration of 1.4mM, which corresponds to 3% crosslinker and 1% initiator molar percentages (relative to monomer).

The suspension turned opalescent in the first minutes and later became white, with a milky appearance. After 3 hours at 70ºC, the reaction was cooled down to room temperature and centrifuged three times at 30,000rpm (92387g) in a Beckman Optima L80-XP ultracentrifuge (Beckman, USA) for 2 hours, for removal of unreacted monomers. The pellet was then resuspended in ultrapure water for further characterization.

2.4.2. Synthesis of core microgels

Core particles of poly(N-Isopropylacrylamide-co-2-dimethylaminoethyl methacrylate), or P(NIPAM-DMAEMA) were synthesized via free radical polymerization based on the work of Shakoori and team.(81) Briefly, 0.250g of NIPAM, 0.010g of Bis, 50µL of SDS 20% solution and 60µL of 2-(dimethylaminoethyl methacrylate) (DMAEMA) were mixed and dissolved in 40mL ultrapure water in a 250mL three-neck round bottom flask. This solution was then heated at 70ºC in a water bath and purged with nitrogen

for 25 minutes while stirring at 300rpm on a magnetic plate. The purge was only started after the temperature was stabilized at 70°C. In parallel, 0.010g of ammonium persulfate (APS) were dissolved in 10mL ultrapure water and equally purged with nitrogen for 15 minutes while stirring at 200rpm on a magnetic plate. After both purges, the APS solution was slowly added to the main reaction (20mL/min). The final reaction would have a NIPAM concentration of 44mM, DMAEMA concentrations of 6.8mM, Bis concentration of 1.30mM, APS concentration of 0.88mM and SDS concentration of 0.87mM, with NIPAM:DMAEMA ratios of 87:13 and molar percentages of 3% crosslinker and 2% initiator (relative to NIPAM).

The suspension turned opalescent in the first 15 minutes and kept this appearance until cooling. After 6 hours at 70°C, the reaction was cooled down to room temperature and centrifuged three times at 30,000rpm (92387g) in a Beckman Optima L80-XP ultracentrifuge (Beckman, USA) for 2 hours, for removal of unreacted monomers. The pellet was then resuspended in ultrapure water for further characterization.

2.4.3. Synthesis of shell microgels

Shell particles of poly[N-Isopropylacrylamide-co-poly(ethylene glycol) methacrylate], or P(NIPAM-PEGMA), were synthesized via free radical polymerization, inspired by the works of Jones and Lyon, and Shakoori and team.(81, 112) Briefly, 0.325g of NIPAM, 0.020g of Bis, 0.025mL of PEGMA and 0.017mL of sodium dodecyl sulphate 20% solution (SDS) were mixed and dissolved in 40mL ultrapure water in a 250mL three-neck round bottom flask. This solution was then heated at 70°C in a water bath and purged with nitrogen for 25 minutes while stirring at 300rpm on a magnetic plate. The purge was only started after the temperature was stabilized at 70°C. In parallel, 0.015g of APS were dissolved in 10mL ultrapure water and equally purged with nitrogen for 15 minutes while stirring at 200rpm on a magnetic plate, to the similarity of the previous syntheses. After both purges, the APS solution was slowly added to the main reaction.

The final reaction would have a NIPAM concentration of 57mM, PEGMA concentration of 1.1mM, Bis concentration of 2.6mM, APS concentration of 1.3mM and SDS concentration of 1.2mM, with a NIPAM:PEGMA ratio of 98:2 and molar percentages of 4.5% crosslinker and 2% initiator (relative to NIPAM).

The suspension turned opalescent in the first 15 minutes and slowly became milky white. After 6 hours at 70°C, the reaction was cooled down to room temperature and centrifuged three times at 30,000rpm (92387g) in a Beckman Optima L80-XP ultracentrifuge (Beckman, USA) for 2 hours, for removal of unreacted monomers. The pellet was then resuspended in ultrapure water for further characterization.

2.4.4. Synthesis of core-shell microgels

Finally, core-shell nanoparticles of poly[(N-Isopropylacrylamide-co-2-dimethylaminoethyl methacrylate)-poly(N-Isopropylacrylamide-co-poly(ethylene glycol) methacrylate], or P(NIPAM-DMAEMA)-P(NIPAM-PEGMA) were synthesized via free radical polymerization, based on the works of Shakoori and team, Gan and Lyon, and Lyon and Jones.(81, 112, 127)

Briefly, 0.486g of NIPAM, 0.020g of Bis, 0.025mL or 0.050mL or 0.075mL of PEGMA, 0.015g of APS and 0.020mL of sodium dodecyl sulfate 20% solution (SDS) were mixed and dissolved in 80mL ultrapure water. This solution was then purged with nitrogen for 30 minutes at room temperature while stirring at 300rpm on a magnetic plate. Simultaneously, 20mL of previously synthesized core particles were heated at 70°C and purged right after with nitrogen for 10 minutes, while stirring in a 250mL three-neck round bottom flask. Then, the main 80mL mix was slowly added to the core particle suspension in parcels, starting by a 30mL addition and followed by 10mL additions each 5 minutes (Fig.4). The suspension was then purged for an extra 10 minutes to ensure a proper nitrogen atmosphere.

The final reaction would have a NIPAM concentration of 43mM, PEGMA concentration of 0.4mM, 0.8mM or 1.7mM, Bis concentration of 1.3mM, APS concentration of 0.75mM and SDS concentration of 0.71mM, with approximate NIPAM:PEGMA ratios of 99:1, 98:2 or 96:4, and molar percentages of 3% crosslinker and 2% initiator (relative to NIPAM).
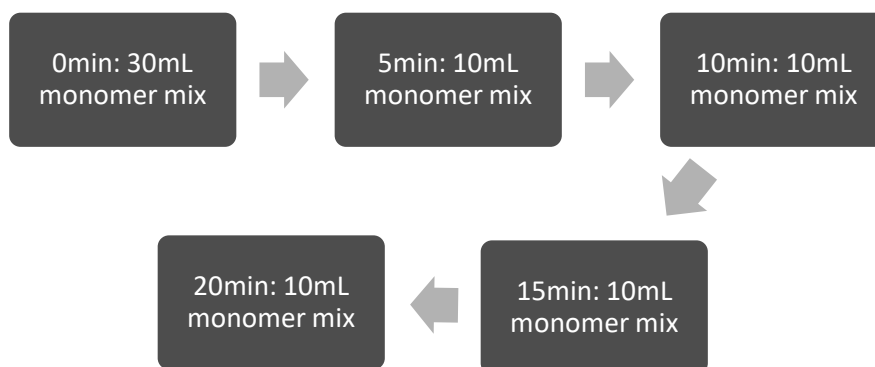
Figure 4. Schematics of monomer mixture addition in the core-shell synthesis protocol. The mixture containing NIPAM, PEGMA, crosslinker and initiator (monomer mix) was added in parcels to the core microgel suspension, in order to properly synthesize the desired shell.

The suspension turned gradually opalescent throughout the process. After 6 hours at 70°C, the reaction was cooled down to room temperature and centrifuged three times at 30,000rpm (92387g) in a Beckman Optima L80-XP ultracentrifuge (Beckman, USA) for 2 hours, for removal of unreacted monomers. The pellet after centrifugation was re-

suspended in ultrapure water or freeze-dried at -80ºC for 3 days in a Virtis BenchTop Pro freeze-drier (SP Scientific, USA) for further characterization.

2.5. Characterization of Polymeric Microgels

2.5.1. Size and surface charge

Much like the ceramic nanoparticles, hydrodynamic diameter and zeta potential measurements for polymeric microgels were performed by dynamic light scattering (DLS) in a Malvern ZetaSizer Nano ZS (Malvern, UK), comprising a He-Ne 633nm wavelength laser with a scattering angle of 173º. The measurements were performed at i3s, Porto, Portugal.

The preparation of the samples was simply carried out by diluting approximately 200µL of microgel suspension pre- and post-centrifugation in 1mL ultrapure water. Three size and zeta potential measurements were made per sample, at 25ºC.

2.5.2. Thermo-responsivity

The thermo-responsive behavior of the microgel was also studied by dynamic light scattering (DLS) in a Malvern ZetaSizer Nano ZS (Malvern, UK) at i3s, Porto, Portugal. The hydrodynamic diameter of the microgels in suspension was studied at different temperatures, from 25ºC to 50ºC with a 5ºC step. Three size measurements were made per sample, per temperature point, with an equilibration time of 120 seconds in between temperature points.

The preparation of the samples was done as described above, by diluting approximately 200µL of microgel suspension in 1mL ultrapure water.

2.5.3. Chemical profile

The chemical profile of the microgels was studied by attenuated total reflectance Fourier transform infrared (ATR-FTIR) spectroscopy in a Perkin-Elmer 2000 (Perkin-Elmer, USA) with a 4cm^{-1} spectral resolution and 32 scans per sample. This measurement was performed at i3s, Porto, Portugal.

A small drop of washed particles in ultrapure water was let to dry in the detector surface and then the measurement was run.

2.5.4. Morphology

Microgels size and shape were assessed by transmission electron microscopy (TEM) in a JEOL JEM-1400 Electron Microscope (JEOL Ltd., Tokyo, Japan) with an accelerating voltage of 120kV and a CCD digital camera Orious 1100W (Tokyo, Japan), similarly to the ceramic nanorods. This analysis was also performed at i3S, Porto. The samples were prepared by diluting the nanoparticle suspensions, usually adding 1mL of ultrapure water to 60-80µL of sample. A 10µL drop was then loaded onto a Formvar/carbon film-coated nickel mesh grid (Electron Microscopy Sciences, Hatfield, PA, USA) for 30 seconds, after which excess liquid was removed with filter paper.

2.6. Encapsulation of hydroxyapatite onto microgels

2.6.1. Mixing method

The first proposed protocol for encapsulation of the nanohydroxyapatite into microgels was the mixing method, which consisted in adding the ceramic nanoparticles to the microgels mid-polymerization. For that purpose, a very similar protocol for the synthesis of core-shell particles was performed. While 20mL of core particle suspension were purged with nitrogen, the same masses of all other reagents (NIPAM, PEGMA, Bis, APS, SDS) were dissolved in 70mL of ultrapure water. Then, 10mL of ultrapure water were used to dissolve 10mg of iron-doped hydroxyapatite (FeHAP), which were then sonicated for 15 minutes in an ultrasonic bath. The addition of FeHAP to the reaction was intercalated with the addition of the NIPAM-PEGMA mixture according to the scheme below (Fig.5). The reaction was performed during 6h at 70ºC, after which the suspension was cooled down to room temperature and stored.

The assessment of the encapsulation degree was performed by TEM on a JEOL JEM-1400 Electron Microscope (JEOL Ltd., Japan), similar to the previously presented particles, also at i3s, Porto, Portugal. The samples were prepared by diluting 60-80µL of composite suspension in 1mL of ultrapure water and a small drop was loaded onto the nickel mesh grids as described before.
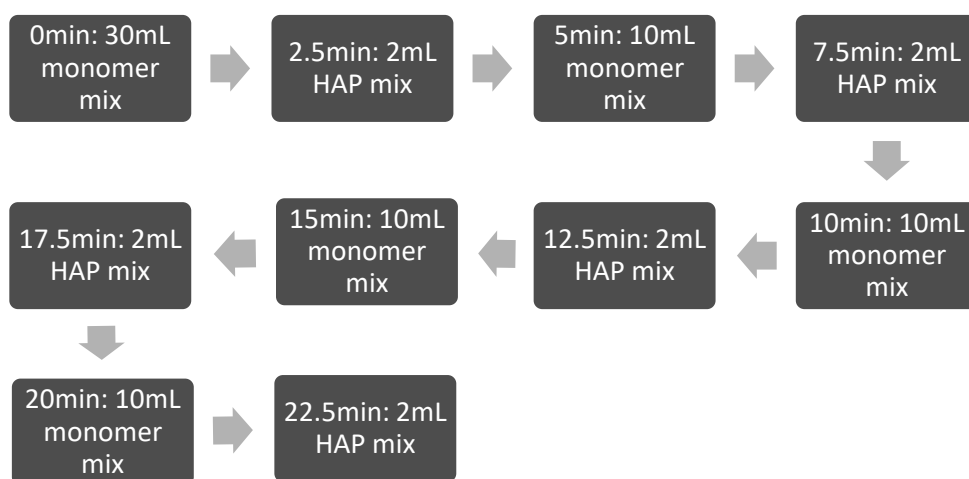
Figure 5. Schematics of monomer/hydroxyapatite (HAP) addition to the mixing protocol for encapsulation of the ceramic particles onto polymeric microgels.

2.6.2. Coating method

The second proposed protocol for encapsulation of the nanohydroxyapatite into microgels was the coating method, which consisted in performing the polymerization around each individual or small agglomerate of FeHAP nanoparticles. With that purpose, a very similar protocol for the synthesis of core-shell particles was performed – after the 10-minute nitrogen purge of the 20mL core particle suspension at 70ºC, 10mg of FeHAP nanoparticles suspended and sonicated in 10mL ultrapure water were added to the reaction. After one minute, 30mL of a total 70mL aqueous mixture of NIPAM, PEGMA, Bis, APS and SDS were immediately added and the reaction was continued. This small pause was long enough to allow a partial nitrogen purge of the FeHAP suspension but sufficiently short as to avoid particle re-aggregation after sonication. Much like the mixing method, the reaction was performed during 6h at 70ºC, after which the suspension was cooled down to room temperature and stored. The assessment of the encapsulation degree was also performed by TEM, as described before.

2.7. Encapsulation of doxorubicin onto microgels

2.7.1. Doxorubicin loading

For the loading of doxorubicin (DOX) into the core-shell microgels, a solution of 0.6mg/mL doxorubicin in phosphate buffer saline (PBS) was prepared. Then, lyophilized core-shell microgels were redispersed in this drug solution to a concentration of

5mg/mL. The suspension was then shaken in an orbital shaker at 4ºC overnight and, after verifying that the microgels were well dispersed, gel filtration was carried out using disposable columns loaded with Sephadex® G-25 gel (GE Healthcare, USA) with a molecular weight cut-off of 25kDa. As a preliminary test, 0.5mL of the drug/microgel sample were loaded into the column and eluted with 6mL PBS over 1.5 days, with a final filtrate of 3mL of non-encapsulated DOX in PBS. The non-encapsulated DOX aliquot was analysed using a Synergy MX fluorimeter (BioTek, USA) at excitation and emission wavelengths of 470nm and 590nm, respectively. PBS was used as blank and a standard curve of DOX was made with the following concentrations: 50 – 20 - 10 - 5µg/mL. The quantification was followed by calculations of the encapsulated efficiency (EE) and drug loading capacity (LC) percentages according to Equations 4 and 5.

$$EE\ (\%) = \ (Mi - Mn)/Mi * 100$$

(4)

$$LC\ (\%) = \ (Mi - Mn)/M\mu * 100$$

(5)

In these equations, *Mi* represents the initial DOX mass in solution, *Mn* represents the non-encapsulated DOX mass in solution, and *Mµ* represents the total microgel mass in solution.

2.8. Cell culture assays

2.8.1. Effect of microgels on the metabolic activity of human gingival fibroblasts

Human gingival fibroblasts (HGF) were cultured in alpha-Modified Eagle Medium (α-MEM) supplemented with 10% (v/v) fetal bovine serum, 1% (v/v) penicillin/streptomycin and 1% v/v Fungizone and incubated at 37ºC at 5% CO_2. Trypsinization and seeding was performed every three days.

As a preliminary test, the metabolic activity of HGF cells in contact with core-shell microgels was assessed by the resazurin assay, first used by Pesch and Simmert.[128] Briefly, metabolically active cells can reduce the blue compound resazurin into resorufin, turning it into a pink-purple appearance that can be detected at an excitation wavelength interval of 540-570nm and an emission wavelength interval of 580-610nm.[129] For this assay, the fibroblasts were trypsinized and seeded onto 96-well plates at a concentration of 5000 cells per well and incubated overnight. In parallel,

freeze-dried core-shell microgels were sterilized in absolute ethanol, dried in sterile conditions and then dispersed in the complete supplemented α-MEM culture at a concentration of 5mg/mL. After overnight incubation, regular medium was exchanged for the microgel-rich medium and the cells were again incubated at 37°C at 5% CO_2. At timepoints of 4 and 24 hours of incubation, each well was loaded with resazurin and re-incubated for 3 hours. The medium was then transferred to a black 96-well plate with transparent bottom and fluorescence was measured at excitation and emission wavelengths of 560 and 590nm, respectively, in a SynergyMX fluorimeter (BioTek, USA).

2.8.2. Effect of microgels on human gingival fibroblast morphology

Fibroblast morphology was also assessed after 4h and 24h-contact with the sterilized core-shell microgels. Briefly, cells were seeded onto a 48-well plate at a density of 3750 cells per well and incubated at 37°C at 5% CO_2 for 4h and 24h. After each timepoint, the wells were washed with PBS and fixed with 4% paraformaldehyde (PFA) solution. After washing 3 times in PBS, the cells were permeabilized with 0.2%(v/v) Triton-X in PBS for 10 minutes while shaking at 50rpm in an orbital shaker. After washing again with PBS, cells were incubated with 1wt% BSA in PBS for 30 minutes while shaking at 50rpm for protein blockage. Next, cells were incubated with AlexaFluor® 488 phalloidin (ThermoFisher, USA) (diluted 100 times in the 1wt% BSA in PBS solution) for 20 minutes stirring at 50rpm in an orbital shaker in dark conditions. Rinsing 3 times with PBS was done once more before incubating the cells with DAPI in PBS at a concentration of 0.1µg/mL for 10 minutes under stirring at 50rpm in an orbital shaker. Finally, the cells were rinsed 3 more times with PBS and their fluorescence was analysed under an Axiovert 200M inverted fluorescence microscope (Zeiss, Germany) at an objective amplification of 10x under a multidimensional acquisition mode of DAPI and AlexaFluor® 488 channels. All steps were performed at room temperature.

2.9. Statistical analysis

Statistical analysis and graphs were made with the GraphPad Prism 5 software (GraphPad, USA) and OriginPro 2018b (OriginLab, USA).

Data are represented as mean ± standard deviation (SD). Normality was not assumed in any condition due to reduced number of repeats. Statistical analysis was performed using Mann-Whitney U test, Kruskal-Wallis test with Dunn's correction for multiple comparisons, and Boltzmann sigmoidal fits, all for conditions with n ≥ 3. Statistical significance was considered when $p < 0.05$ and represented with * for $p < 0.05$, ** for $p < 0.01$ and *** for $p < 0.001$.

(page intentionally left blank)

Chapter III

Results and Discussion

3.1. Characterization of Ceramic Nanoparticles

3.1.1. Size, surface charge and morphology

The size, shape and charge of a nanoparticle influence several aspects at the biological level, namely cell uptake and particle toxicity. As such, it is important to characterize all biomedical nanomaterials to better predict their behaviour *in vivo*.

Wet chemical precipitation of hydroxyapatite nanoparticles commonly suggests the use of surfactants, either for shape determination or for particle separation, which may difficult the doping process. In any case, surfactants and stabilizers are still vital after synthesis, especially for the separation of the grains and agglomerates in suspension for characterization purposes such as DLS and TEM. Past studies have explored several solutions, such as potassium chloride(130) or sodium dodecyl sulphate(100), but in this work sodium citrate proved the ideal stabilizer for hydroxyapatite (HAP) and iron-doped hydroxyapatite (FeHAP) nanoparticles. Sodium citrate was tested at stabilizer:particle weight ratios of 0.5, 1 and 2, with the ratio of 1 being the most successful in terms of dynamic light scattering (DLS), polydispersity index (PdI) and shelf-life results (*see Appendix A*).

Regarding shape, nanoparticles with higher aspect ratios usually report higher rates of cell internalization(131), so the hydroxyapatite synthesis was planned with the purpose of obtaining needle- and rod-like particles, as done in previous works.(59, 130)

As for surface charge, it is important to analyse particles in their individual form in order to increase the effective surface area and thus obtain accurate zeta potential measurements. Notably, the vast majority of samples for zeta potential is dispersed in

buffers or in solutions containing surfactants or stabilizers prior to analysis. In general, colloidal suspensions with a zeta potential modulus higher than 30mV are considered very stable and with a long shelf-life. For hydroxyapatite, surface charges from -10mV to -25mV have been reported in phosphate buffers(132, 133) and -8mV and -9mV for 0.01M KNO_3 and 0.01M NaCl, with the best result of -32mV for 0.01M KCl.(130)

In the present work, undoped hydroxyapatite (HAP) nanorods showed a hydrodynamic diameter of (164 ± 3.89) nm in DLS, while on TEM the particles showed a length range of 20-100 nm and a width range of 12-24 nm; iron-doped hydroxyapatite (FeHAP) showed a more variable DLS size of (284 ± 18.5) nm and TEM size ranges of 20-80 nm for length and 6-18 nm for width (Table 4, Figs.6-8). Even after the use of sodium citrate, agglomerates were still detected both in TEM and DLS, particularly in the case of FeHAP (Fig.6.A). The random manner of aggregation and the different aspect ratios of the particles (2.5 for HAP and 5.0 for FeHAP, Fig.7) seen in TEM may account for the considerable differences between HAP and FeHAP observed in DLS and zeta potential results. Curiously, DLS measurements of particles stabilized in sodium citrate showed a polydispersity index (PdI) close to 0.2, a satisfactory indicator of particle homogeneity in solution.

Table 4. Hydrodynamic size and surface charge measurements of hydroxyapatite (HAP) and iron-doped hydroxyapatite (FeHAP) stabilized with sodium citrate (NaCit) at a weight ratio of 1, at 25°C. Results represented as mean ± standard deviation (n=2 for size, n=3 for zeta potential).

Sample	Polydispersity Index	Z-average (nm)	Main Intensity Peak (nm)	Zeta Potential (mV)
NaCit:HAP	0.207 ± 0.008	135 ± 2.33	164 ± 3.89	-39.9 ± 2.11
NaCit:FeHAP	0.246 ± 0.000	214 ± 4.38	284 ± 18.5	-33.0 ± 0.874
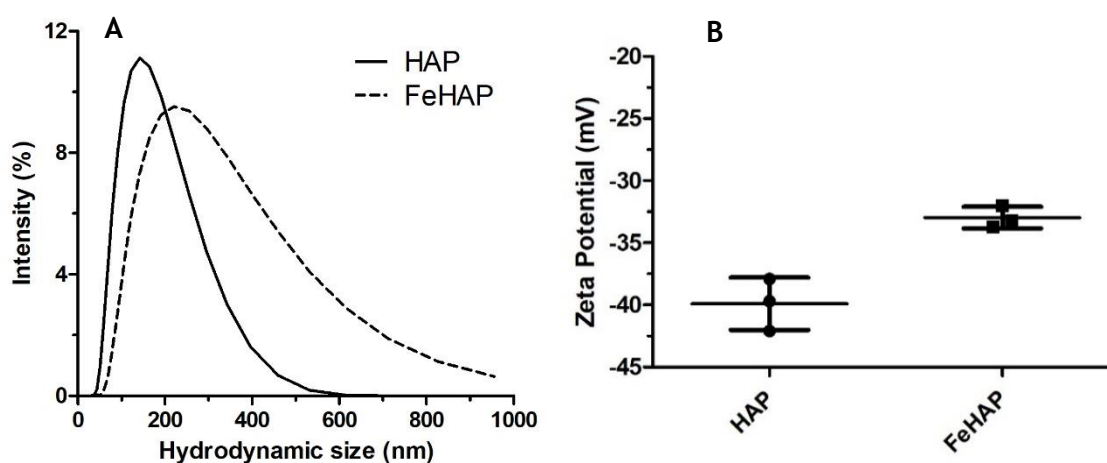
Figure 6. Hydrodynamic size (**A**) and surface charge measurements (**B**) of hydroxyapatite (HAP) and iron-doped hydroxyapatite (FeHAP) stabilized with sodium citrate (NaCit) at a weight ratio of 1. Zeta potential results represented as mean ± SD (n=3), with p=0.1000 (Mann-Whitney U test).
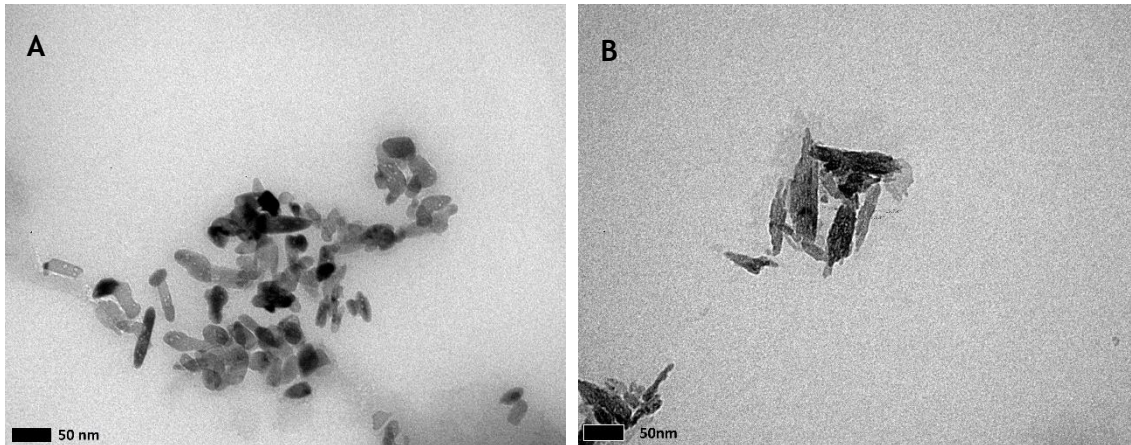
Figure 7. Representative TEM pictures of HAP (**A**) and FeHAP (**B**) stabilized in sodium citrate at a stabilizer:particle weight ratio of 1. Scale bars: 50nm. Amplification: 200000x.
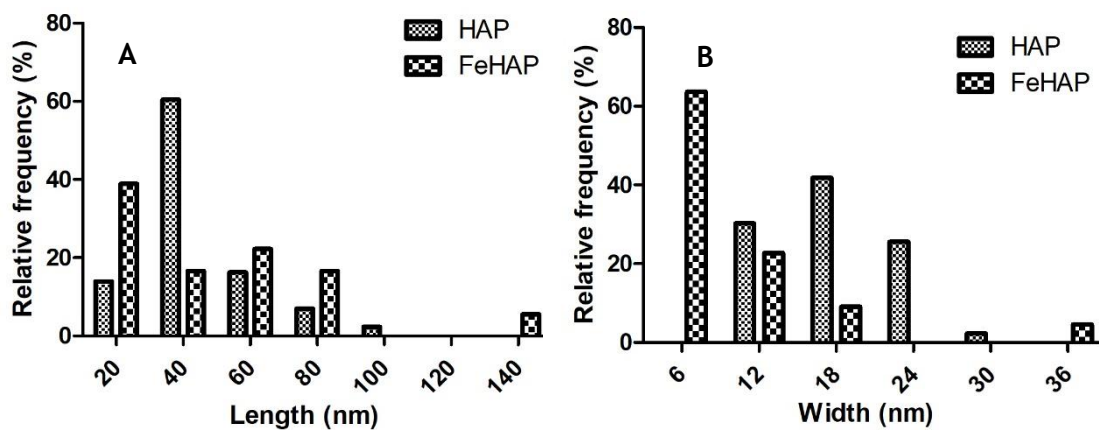
Figure 8. Undoped (HAP) and iron-doped hydroxyapatite (FeHAP) length (**A**) and width (**B**) frequency distribution as seen in TEM images.

Zeta potential measurements of both samples were (-39.9 ± 2.11) mV for HAP and (-33.0 ± 0.874) mV for FeHAP (Table 4). Both are below -30mV, hinting at relatively stable nanoparticle suspensions when sodium citrate is employed, although some aggregates should be further separated through sonication.

In sum, DLS and TEM results showed different sizes for the HAP and FeHAP nanoparticles. In suspension, the nanoceramics proved to be rather stable in structures under 300 nm stabilized by sodium citrate; the present size interval is, however, still too high for FeHAP, and so more intense separation methods should be attempted. Differences in particle shape (rod vs. needle) can also be overcome with a more rigorous

temperature control.(102) In any case, the needle-like shape of FeHAP may be advantageous, seen that a) the nano-needles are much readily uptaken by the cells, and b) are expected to show more cytotoxicity, which may be beneficial for cancer therapy applications if released directly in the tumour milieu. Lastly, sodium citrate seems to be an excellent stabilizer for these nanoceramics, which could be employed *in vitro* and *in vivo* with possible added benefits in the reduction of cytotoxicity of particles in circulation.(134)

3.1.2. Chemical profile

The conduction of chemical profile analyses is important to assess the occurrence of contaminations and to help better understand the findings of other chemical characterization studies such as X-ray diffraction. Raman spectroscopy and FTIR are two complementary chemical profile methods that, when combined, provide solid proof of the chemical identity of a sample. Hydroxyapatite can be identified by its main vibrational modes of PO_4^{3-} and OH^-, with the possibility of some water and carbonate contaminations.(59, 100, 135)

In the present FTIR analysis (Fig.9), the spectra corresponding to hydroxyapatite O-H stretching can be found at ~3570cm^{-1} in all samples, although very faint in the iron-doped material, and the vibrational O-H peak at 634cm^{-1} can only be found in sintered undoped HAP. A broad band and a noticeable peak associated with water are found in all samples at ~3435cm^{-1} and ~1635cm^{-1}. Residual carbonates incorporated from CO_2 can be found at ~1470 cm^{-1}, ~1421cm^{-1} and ~874cm^{-1} in the non-sintered samples. Lastly, the four modes of PO_4^{3-} can be detected in all samples. The *v1* mode can be detected at ~961cm^{-1}, although more faintly in FeHAP samples; the *v2* mode may be seen at ~470cm^{-1}; the *v3* mode can be observed at ~1035cm^{-1} and ~1090cm^{-1}, more easily in the sintered samples than in the non-sintered material, with no distinguishable third peak at 1110cm^{-1} in any of the samples; and the *v4* mode can be very clearly observed at ~565cm^{-1} and ~603cm^{-1} in all samples *(see Appendix A for more detail)*.

From the analysis, it can be inferred that non-sintered samples have more tendency to incorporate CO_2 than sintered ones, simply due to the fact that this heating process consolidates the lattice, reduces porosity and therefore makes it less permeable to gas incorporations. Residual water is naturally present in every sample, usually incorporated during the preparation of KBr discs. The incorporation of iron in the lattice could not be detected by this analysis. Regarding PO_4^{3-} and OH^- peaks, most samples seem to show the calcium phosphate peaks - however, due to its faintness in the iron-doped samples, Raman spectroscopy was performed to confirm these results.

Figure 9. Fourier transform infrared spectra of sintered (*sint*) and non-sintered hydroxyapatite (HAP) and iron-doped hydroxyapatite (FeHAP). Curves are represented in order and according to the legend. Vertical offset was adjusted for individual curve analysis. One measurement per sample was performed.
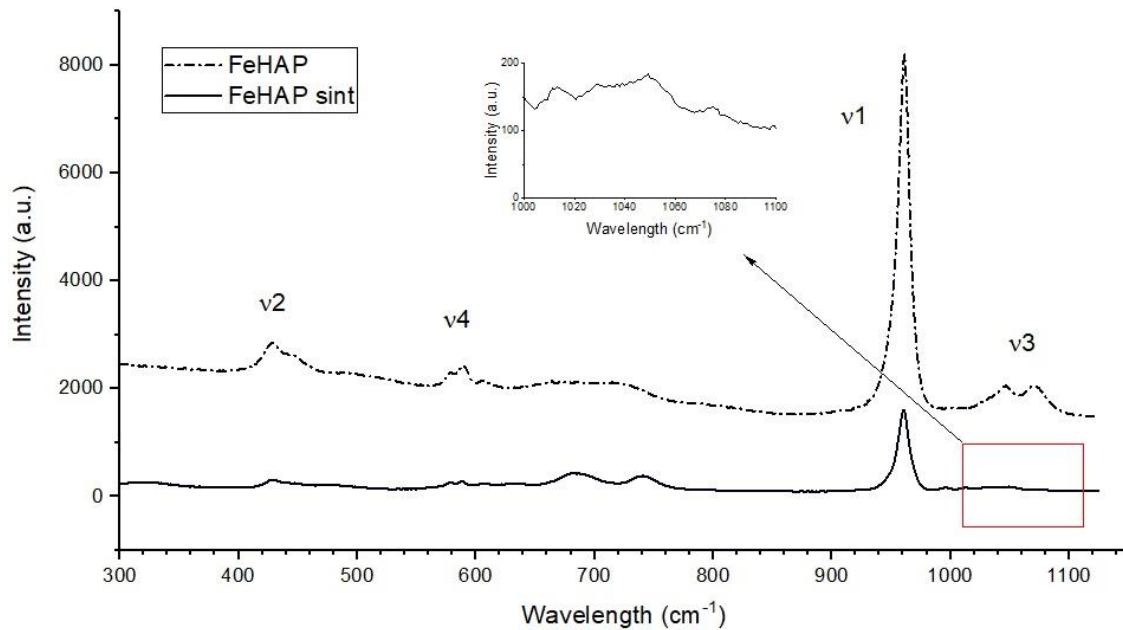
Figure 10. Raman spectra of sintered and non-sintered iron-doped hydroxyapatite (FeHAP). Phosphate vibrational modes are identified above each correspondent peak(s). Curves are represented in order and according to the legend. One measurement per sample was performed, with acquisition times of 1200s for *FeHAP* and 60s for *FeHAP sint*.

The analysis of both Raman spectra for sintered and non-sintered FeHAP lead us to conclude that both samples exhibit the *v1, v2,* and *v4* peaks relative to phosphate vibrational modes (Fig.10). The *v3* duplet identifiable through Raman spectroscopy, however, remained weak in sintered FeHAP (Fig.10, inset). Penel reported the *v3* group as unstable, hence the difficulty in its detection, so it would be interesting to repeat the sintered measurement at longer acquisition times.(135) Most notably, additional peaks were detected at ~685 and ~740cm^{-1} in both samples, more intensely and clearly in the sintered sample. This signal is thought to correspond to iron oxide.(136) Indeed, from the literature, it could be understood that these small signals most likely correspond to small maghemite formations.(137)

To conclude, all samples appear to be calcium phosphates, with iron-doped samples having additional iron oxide portions, most likely maghemite. Depending on the size of these phases, their presence may bring interesting magnetic properties, especially superparamagnetism, conferring potential for T2 contrast imaging in MRI.

3.1.3. Crystallinity

Crystalline phase analysis through X-ray diffraction (XRD) reveals information on the crystallinity, the type of crystal structure and the presence of other crystal phases in a sample. From the results of this procedure, it is not uncommon to find other calcium phosphate phases associated to sintered nanohydroxyapatite, most commonly α-TCP and β-TCP.(59, 100) This is generally attributed to an incomplete reaction of all reagents, especially the OH^{-} groups which distinguish hydroxyapatite from tricalcium phosphates.

In the present work, both sintered and non-sintered HAP and FeHAP were studied by XRD analysis. All samples showed the typical peaks corresponding to hexagonal hydroxyapatite (Fig.11), as expected, with sintered FeHAP showing similarities to melonjosephite, a mineral containing calcium, iron, phosphates and hydroxyl groups. Furthermore, it was shown that all sintered samples had small amounts of TCP phases. Although TCP peaks are not visible in the non-sintered materials, it is most likely that these materials do not correspond to pure HAP either. Sintered FeHAP presented only a small α-TCP contamination while sintered HAP presented both α-TCP and β-TCP. Non-sintered samples are more amorphous than sintered samples, given that sintering compacts the material into a solid, more organized and consequently more crystalline structure. This can be inferred from the width of the peaks (Fig.11).
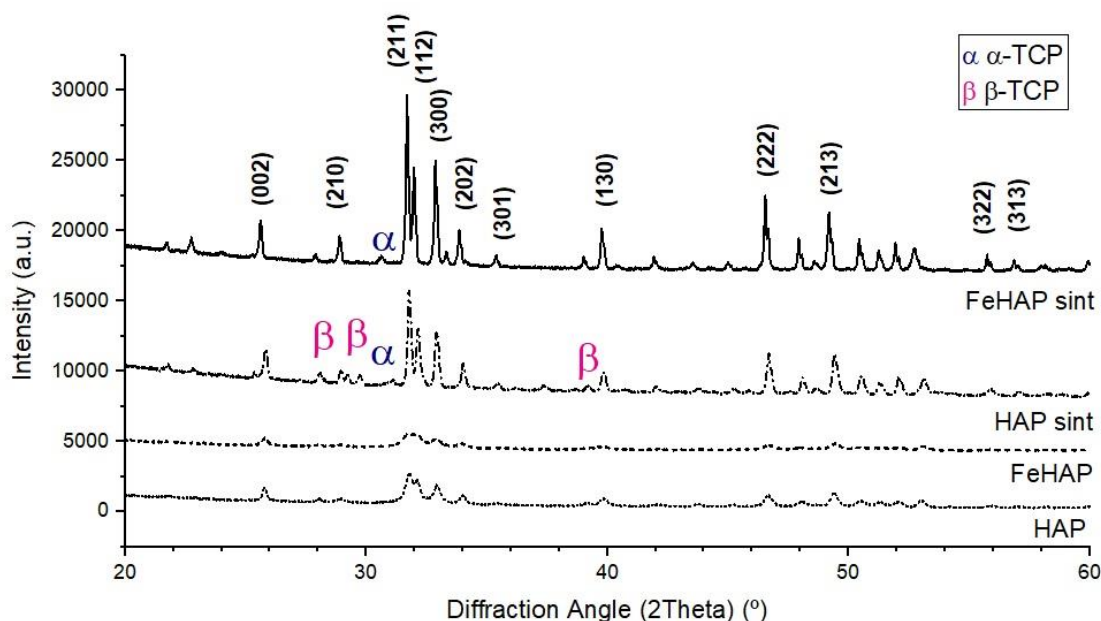
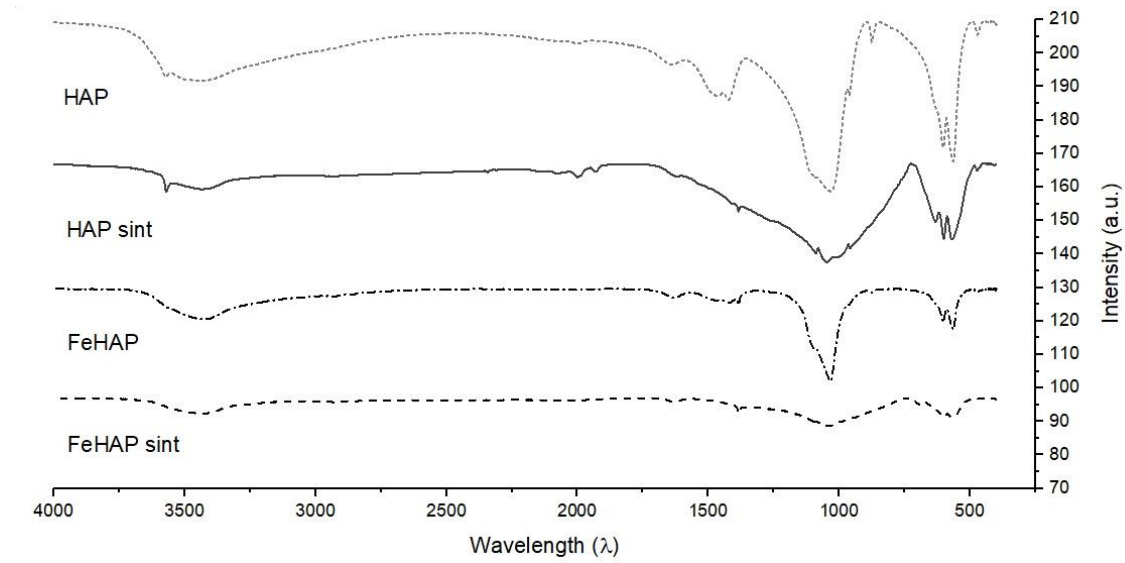**Figure 11.** XRD diffractograms of sintered (*sint*) and non-sintered hydroxyapatite (HAP) and iron-doped hydroxyapatite (FeHAP). Curves are represented in order and according to the legend. Vertical offset was adjusted for individual curve analysis. α and ß represent the peaks corresponding to residual α- and ß-tricalcium phosphate (α-TCP and ß-TCP). Numbers between parentheses represent the three dimensional parameters of the typical lattice planes observed in HAP, as indicated by data from the International Crystallography Diffraction Database (ICDD).

As suggested from the Raman results, the present XRD diffractograms were analysed for the detection of iron oxide signals.(138) No conclusive correlation was found between the samples and the iron oxide spectra found in the literature, given that the most intense peak in magnetite and maghemite occurs at $2\theta \sim 36°$ and may overlap the (301) peak of HAP (Fig.11).(57) As such, the presence of magnetite/maghemite cannot be accurately confirmed by XRD. Fortunately, Raman spectroscopy is more sensitive to the detection of certain compounds than other chemical analysis techniques, and so other ways of confirming the presence of magnetite and maghemite should be conducted, for instance through energy dispersive X-ray spectroscopy (EDS).

The conclusion from XRD is that all samples are mostly hydroxyapatite, with some expected TCP phases. Additionally, the formation of some iron oxide phases was not discarded despite XRD not being conclusive on this matter. Up until now, the destiny of Fe^{3+} irons during the synthesis could not be clearly attributed to an incorporation in the HAP lattice or an incorporation into magnetite/maghemite. However, from previous descriptions, considering the pH and temperature of the synthesis process, it is likely that Fe^{3+} was considerably uptaken by the iron oxide structures.(57) Again, EDS would shed some light on this issue.

From a biochemical point of view, the presence of TCP is not necessarily unfavourable - tricalcium phosphates degrade more easily in physiological environments than HAP, and α-TCP solubilizes faster than ß-TCP.(139) Therefore, there is a great possibility that Ca^{2+} ions may be liberated in larger quantities, possibly contributing to the desired disruption of the calcium homeostasis of the cancerous cells, in addition to other anti-cancer effects previously reported for nanoHAP such as protein synthesis inhibition and cell cycle arrest.(19)

3.1.4. Magnetic properties

From Raman spectroscopy, both sintered and non-sintered FeHAP indicated the presence of iron oxide phases. Should they prove superparamagnetic, their potential for T2-weighted MRI contrasting would be strengthened. As such, the magnetic properties of both sintered and non-sintered FeHAP were assessed.

Average superparamagnetic iron oxide nanoparticles show saturation magnetizations (M_s) around 50-60emu/g.(140) Naturally, iron-doped nanoHAP is expected to yield lower values, with Tampieri producing iron-doped hydroxyapatite with M_s ~2emu/g and ~4emu/g(57), and Gloria producing materials with 30% FeHAP with an M_s between 0.5 and 1emu/g.(58) Curiously, both works report not just superparamagnetism but also a slight hysteresis loop, possibly due to ferrimagnetic magnetite phases. Laranjeira and Moço also described the M_s of sintered iron-doped hydroxyapatite nanoparticles between 0.5 and 1 emu/g.(59)

Much can be inferred from the careful analysis of Figure 12. Interestingly enough, sintered and non-sintered samples showed completely different magnetic behaviours, with the first appearing to be superparamagnetic and the latter appearing paramagnetic.

Firstly, the paramagnetism of non-sintered FeHAP allied to its low M_s predict a negligible magnetically-induced heating effect and an inability to perform as a T2-weighted MRI contrast agent. The sintered sample, despite showing low M_s (0.5emu/g), reported superparamagnetism, and consequently proved its potential as a contrast agent.

While superparamagnetism is mostly attributed to single magnetic domains of some iron oxides, it may also be that single domains of Fe^{3+} incorporated in the HAP lattice contribute to this.(57) Furthermore, a small hysteresis loop can be detected in the sintered sample, indicating slight ferri- or ferromagnetism (Fig.12, inset). This ferrimagnetism may derive from multi-domains of maghemite, but multi-domains of Fe^{3+}-incorporated HAP may also contribute to it. In sum, sintered FeHAP possesses both superparamagnetic and ferrimagnetic properties, both possibly due to maghemite and

Fe^{3+} incorporated in the HAP lattice, with the differentiating factor being the type (and size) of the magnetic domain.

For T2-weighted MRI contrasting, sintered FeHAP proved more promising than non-sintered FeHAP. This material would be a good alternative to currently employed superparamagnetic iron oxide nanoparticles (SPIONs) in T2 contrast imaging in MRI, in the sense that the superparamagnetic characteristics would be maintained and the complications of having iron-based materials in the bloodstream would be mostly reduced. One limitation, however, is its poor solubility in water, which can be overcome with the application of stabilizers such as sodium citrate and ultrasonication. Magnetic hyperthermia studies would also be an interesting follow-up on this section.
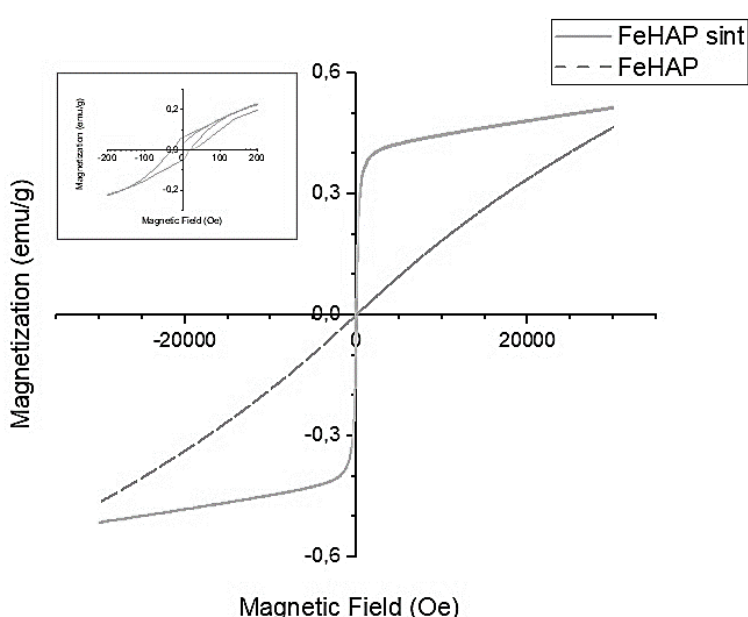
Figure 12. SQUID characterization of sintered (FeHAP *sint*) and non-sintered iron-doped hydroxyapatite (FeHAP) nanoparticles. One measurement was made per sample. Inset: sintered FeHAP behaviour at a neutral external magnetic field.

3.2. Synthesis optimization of polymeric microgels

It is widely accepted that the production of particles at the nanoscale is dependent from local, environmental, chemical and many other parameters during their synthesis. While some protocols are not considerably affected by these factors, others have a clear dependency. In this study, a striking contrast between the reproducibility of each microgel synthesis protocol was evident, with processes involving the polymerization of DMAEMA being the most susceptible to changes in external factors, as explained in the next sections.

3.2.1. Optimization of the synthesis of core microgels

The first part of the optimization process of the copolymerization of NIPAM and DMAEMA consisted in adjusting the NIPAM:DMAEMA ratios originally suggested by Shakoori et al.(81), so as to produce core nanoparticles with a VPTT between 38ºC and 39ºC and a hydrodynamic size lower than 250nm at 25ºC. After numerous adjustments, the properties of the microgel were only within the desired range a few times, with flocculation often occurring mid-synthesis. In other words, there was an extreme difficulty in reproducing the protocols, partially attributed to the cationic nature of DMAEMA and the anionic nature of other reagents, namely SDS and APS. A protocol without the surfactant SDS was also tested, only to yield intense flake formation during synthesis. To the best of our knowledge, the literature only reported the use of anionic reagents with DMAEMA. Nevertheless, an interesting future alternative would be to use cationic surfactants and initiators and compare reproducibility with the original protocol.

Table 5. External parameters adjusted to the same core particle protocol, attempted variations and best result for each.

External parameter	Variations	Best result
Stirring speed (rpm)	200; 300; 350	200
N$_2$ purge time (pre-initiator) (min)	5; 10; 15; 25	25
N$_2$ purge time (post-initiator) (min)	5; 10	Until opalescence is observed
Initiator addition rate (mL/min)	10; 20; 40	20
Surfactant volume (µL)	0; 30; 60; 120	60
Time of reaction (h)	3; 6	6

In any case, to find ways to solve these inconsistencies, several external parameters were adjusted for the same protocol (Table 5). Despite the outstanding transfection properties of DMAEMA, other tertiary amine monomers such as N-[3-(dimethylamino)propyl] methacrylamide (DMAPMA) could also be used, although their transfection properties would still need to be further confirmed.

3.2.2. Optimization of the synthesis of core-shell microgels

The synthesis of the final core-shell particles was adapted from the work of Jones and Lyon to the core particles hereby developed.(112) Despite the difficulty in core production, the core-shell protocol was fairly reproducible, easily adaptable, and yielded more homogenous batches than the intermediate (core and shell) steps. Three volumes of PEGMA were tested, with 0.025mL, 0.050mL and 0.075mL, all reporting equally good results.

3.2.3. Microgel integrity after lyophilization

One of the main concerns in microgel production is the conservation process. Lyophilization is a widely used technique to remove water from a sample through sublimation and transform it into a powder-like product, making its distribution and use for further applications easier. However, lyophilization is also known to change the physical properties of more sensitive particles, given its extreme temperature and pressure conditions. To assess the integrity of the core-shell microgels, the size and thermoresponsivity of a core-shell batch (centrifuged) was assessed pre- and post-lyophilization.

Table 6. Volume phase transition temperatures (VPTT) of core-shell microgels before (*core-shell centrif.*) and after lyophilization (*core-shell centrif. + lyoph.)*. Data represented as mean ± SD (n=2 measurements per batch).
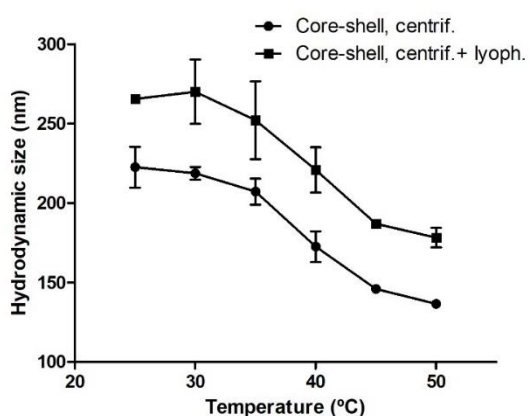
Sample (no. of batches)	VPTT (ºC)
Core-shell centrif. (n=2)	39.2 ± 0.700
Core-shell centrif. + lyoph. (n=2)	39.0 ± 2.28

Figure 13. Temperature trend curves for core-shell microgels before (*core-shell, centrif.*) and after lyophilization (*core-shell, centrif.+lyoph.).* Lyophilized powders were dissolved in ultrapure water for analysis. Data represented as mean ± SD (n=2). Boltzmann sigmoidal fit was performed to assess the V50 value (equivalent to VPTT).

As observed in Figure 13, the lyophilized sample showed an overall higher particle size. Regarding thermoresponsivity (Table 6), both samples showed similar VPTT values with no significant difference (p=0.7580, Boltzmann sigmoidal fit). Notwithstanding this evidence, the analysis of a wider number of samples would allow more solid conclusions.

To sum up, lyophilization appears to solely aggregate the material, without altering its physical properties. In any case, more samples should be analysed in DLS to confirm this inference. Other results for lyophilized powders are presented in the next sections, namely zeta potential and FTIR, which also support the conclusion that lyophilization aggregates the microgels. For the purpose of this work, lyophilization was useful in preparation for following steps such as cell culture assays, but safer alternatives should be sought while still in a product development phase.

3.3. Characterization of polymeric microgels

3.3.1. Size and thermoresponsivity

Once again, the aim of this work regarding the production of polymeric microgels would be to obtain thermo-responsive spherical microparticles with a maximum size of 250nm at 25ºC and a volume phase transition temperature (VPTT) between 38ºC and 39ºC. Throughout the synthesis of the final nanoparticles, intermediate syntheses were conducted to assess the properties of each individual portion. The intermediate steps include the production and characterization of core and shell particles.

Firstly, PNIPAM showed a VPTT of (35.0 ± 0.092)ºC, different from the 32ºC commonly found in the literature (Fig.14.A). This phenomenon can be explained by the crosslinking degree and, most notably, the concentration of SDS. At lower crosslinking degrees, polymer chains are more separated and consequently their repulsive forces are weaker, leading to an augmented LCST.(141) In the case of SDS, at T < LCST, it is believed that SDS molecules form micelles within the polymer matrix and further stretch it. It has been shown that SDS concentrations of 1.42mM can shift the LCST of PNIPAM to values close to 37ºC.(142)

The syntheses of core microgels yielded very different results with different sizes (Fig.14.B), due to the difficulty in reproducing this protocol. Its thermoresponsivity, however, did not vary much as the VPTT kept at an average of (40.8 ± 0.739)ºC (Table 7). As mentioned before, the final core-shell particles reported much more homogeneous sizes (Fig.14.D), possibly due to the stabilizing effect of PEGMA. In other words, these distinct cores did not radically affect the desired outcome.

Table 7. Hydrodynamic size, polydispersity index (PdI) and volume phase transmission temperature (VPTT) of several batches of PNIPAM, core, shell, and core-shell microgels at 25°C. Data represented at mean ± SD (n= number of analysed batches).

Sample (no. of batches)	PdI	Hydrodynamic size (nm)	VPTT (°C)
PNIPAM (n=2)	0.048 ± 0.013	185 ± 6.15	35.0 ± 0.092
Core (n=4)	0.407 ± 0.117	295 ± 43.6	40.8 ± 0.793
Shell (n=3)	0.127 ± 0.044	365 ± 57.2	37.5 ± 0.503
Core-shell (n=3)	0.133 ± 0.020	217 ± 17.2	38.6 ± 0.153

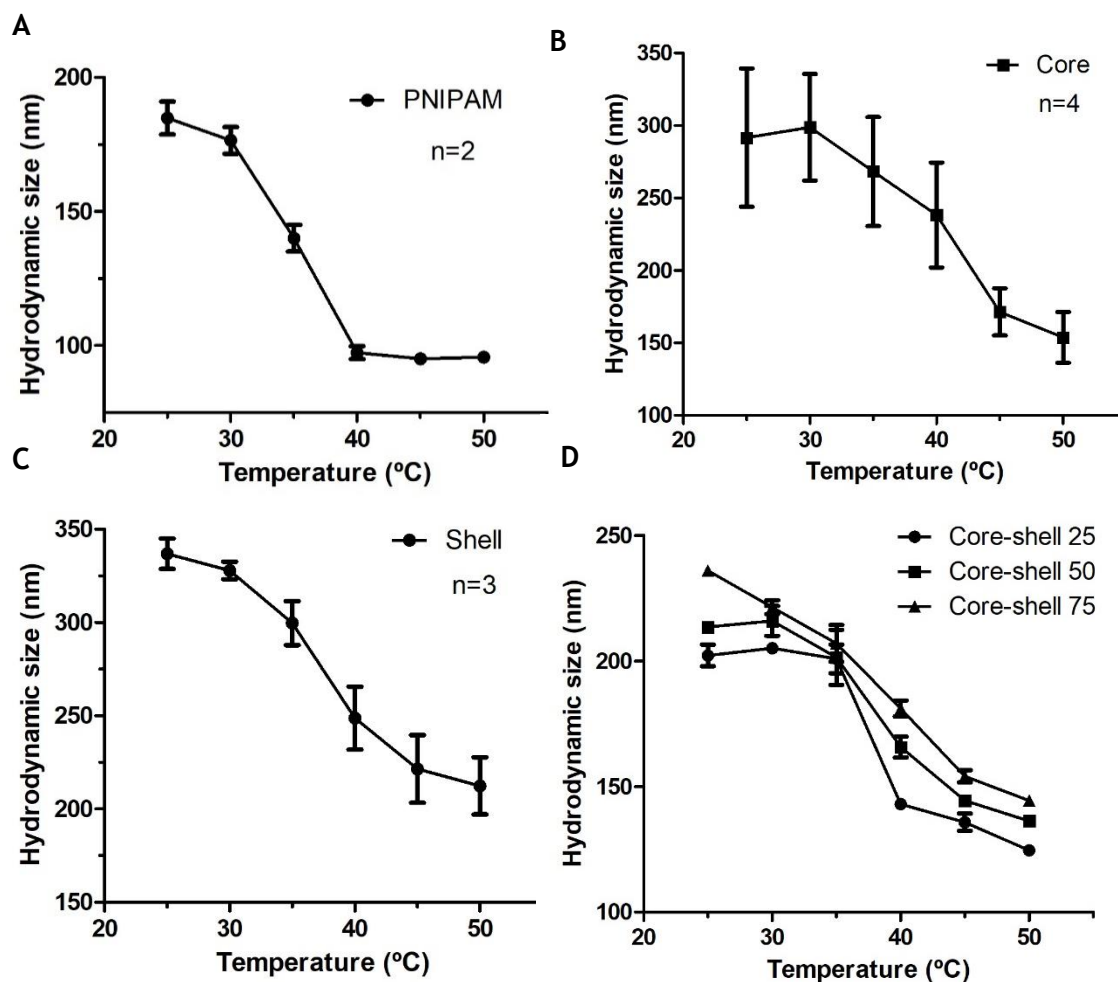**Figure 14.** Temperature trend curves for PNIPAM (**A**), core (**B**), shell (**C**), and core-shell microgels synthesized with either 25, 50, or 75 µL PEGMA (**D**). All are presented as the average temperature curve for n batches except for core-shell microgels. Data represented as mean ± SD (n= number of batches of each type of microgel). Boltzmann sigmoidal fit analysis were conducted for V50 (VPTT) comparisons.

Shell microgels showed very homogeneous batches with regard to both size (PdI < 0.2) and VPTT (Fig.14.C, Table 7). The main focus of the analysis of shell particles would be to compare their VPTT with those of the final microgels, as a way to infer about the proper formation of a shell around the cores.

Lastly, concerning core-shell particles (Fig.14.D), all batches showed excellent size homogeneity and VPTT values between the narrow range of 38.4°C and 38.7°C - located between the average values for core and shell microgels, as desired (Table 7). This is an indication that P(NIPAM-DMAEMA) is present in the nuclei. To further complement this assumption, curve fit comparisons were made between the VPTT of all types of microgels. These revealed non-significant differences between the VPTT of core-shell and core microgels (p=0.4136) and between the VPTT of core-shell and shell microgels (p=0.4346). In contrast, there were significant differences between the VPTT of PNIPAM and the final microgels (p=0.0044). All these observations hint at a final particle containing both P(NIPAM-DMAEMA) and P(NIPAM-PEGMA).

To sum up, we successfully obtained homogeneous core-shell particles with hydrodynamic sizes of approximately 220nm at 25°C and an average VPTT of 38.6°C, within the initially aimed interval. In microenvironments at temperatures above the VPTT, the load of the microgels is expected to be easily released. Concerning size, these nanocarriers would have diameters lower than 200nm at regular body temperature, thus not posing a risk of emboly. Additionally, due to their size, there is a higher probability of these microgels being more easily uptaken by cells.

3.3.2. Surface charge

To assess the net result of all the charge interactions within the microgels, their surface charge was assessed through zeta potential. Two temperatures, one below (25°C) and other above (40°C) the LCST of the microgels were tested, with the purpose of evaluating the zeta potential of these particles under heated environments.

According to the literature, PNIPAM is quite neutral, with surface charges between 0 and -5mV at 25°C but values as low as -30mV at 40°C, in the syntheses where anionic initiators were used.(143) Nevertheless, the initiator is not just the only factor contributing to these changes - when the microgel contracts to its globular form, the charge per surface area tends to increase and the hydrophilic groups tend to expose themselves. In the present work, even though an anionic initiator was employed in all syntheses, the phase transition of such intricate polymeric matrices does not translate into such clear differences in average surface charge.

Table 8. Zeta potential of PNIPAM, core, shell, aqueous suspension core-shell and lyophilized core-shell microgels at 25°C and 40°C, after centrifugation. Data represented at mean ± SD (n= number of measurements).

Sample	Zeta potential 25°C (mV)	Zeta potential 40°C (mV)
PNIPAM (n=2)	-14.3 ± 4.24	-19.9 ± 2.90
Core (n=3)	-4.3 ± 0.86	-4.9 ± 2.1
Shell (n=3)	-25.6 ± 5.63	-27.2 ± 6.03
Core-shell, aq. (n=4)	-22.6 ± 4.16	-21.3 ± 3.25
Core-shell, lyophilized (n=3)	-15.3 ± 3.80	-17.2 ± 2.82
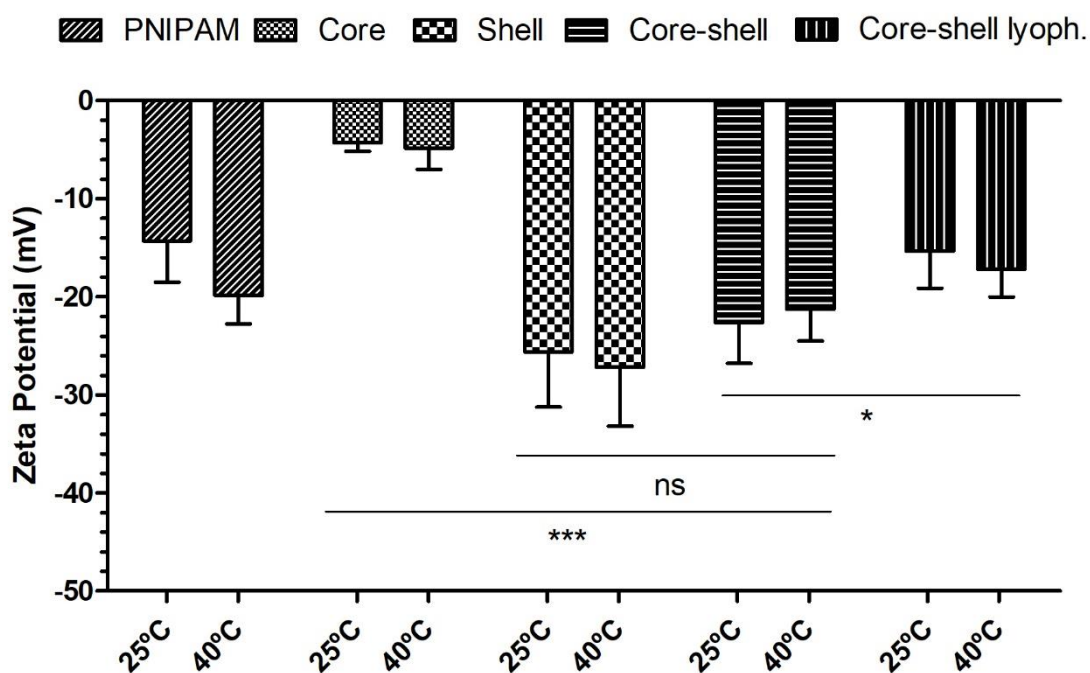
Figure 15. Zeta **potential of** PNIPAM, core, shell, aqueous suspension core-shell and lyophilized core-shell microgels at 25°C and 40°C, after centrifugation. Data represented at mean ± SD (n= number of measurements presented in Table 7). Kruskal-Wallis test with Dunn's correction for multiple comparisons was performed for copolymeric types of microgel only. Ns: non-significant; *: $p < 0.05$; ***: $p < 0.001$.

Firstly, none of the microgels herein presented decreased its surface charge as steeply as the PNIPAM described in the literature (Table 8, Fig.15).(144) The main

reasons for this are a) the proximity of all VPTT values to 40ºC, indicating that the phase transition may still be occurring at this temperature; and b) the fact that SDS was used during all syntheses. Briefly, when a microgel with SDS micelles entrapped in its matrix is heated, the volume phase transition is believed to follow two steps: the first entails the exit of SDS micelles, and the second involves the polymer chain contractions *per se*. This translated into a much slower transfiguration and, therefore, not very drastic changes in surface charge.

Not surprisingly, core particles reported the surface charge closest to zero, due to the cationic nature of DMAEMA. Shell particles exhibited the most negative surface charge due to the presence of PEGMA and its OH$^-$ termination facing outwards in aqueous solutions. These values were not significantly different from the core-shell particles (p>0.05), further suggesting that the final microgels include the outer shell.
Core-shell microgels proved to be more negative than core particles but slightly more positive than shells, corroborating the presence of DMAEMA in the nuclei. Interestingly, this type of microgels is the only one in which surface charge increases at 40ºC – indeed, at this temperature, the anionic chains of the shell are contracted, exposing the cationic groups of the core. Lastly, lyophilized core-shell microgels have shown a significantly different, less negative zeta potential when compared to non-lyophilized samples. This confirms that the extreme conditions of lyophilization tend to aggregate these nanoparticles.

In short, the lower zeta potentials at 40ºC indicated a reduced probability of particle aggregation in all types of particles except for the core-shells. At 40ºC, the cationic groups are slightly exposed, possibly causing more toxicity than the more negative forms at lower temperatures. With this, more cancer cells can be reached by these polymeric carriers, with an enhanced uptake and more effective cell death.

3.3.3. Morphology

The appearance and shape of the microgels were assessed through TEM. Most studies in the literature regarding this type of copolymer microgels do not include a TEM analysis; in fact, only PNIPAM and some copolymers has been evaluated in terms of electron microscopy.(145, 146) Having in mind the low crosslinker percentage of the hereby developed microgels, it is not unlikely to hypothesize that the vacuum to which the sample is submitted may disrupt the particles. In any case, to assess the actual reason behind this, a TEM study was conducted, with PNIPAM particles for comparison.

Many artifacts could be seen in these images. It is believed that these may correspond to unwashed foreign particles (Figs.16.A), or to the expected rupture effect (Figs.16.B-D). The least damaged sample was PNIPAM due to the more uniform and well-known synthesis (Fig.16.A). The most damaged sample was, naturally, the one corresponding

to the core microgels, due to their very heterogeneous synthesis (Fig.16.B). The most important detail to notice, however, is that most particle size did not correspond to the size obtained by DLS (core-shell: ~80nm in TEM compared to ~220nm in DLS). This effect may be due to water removal during sample preparation and/or interactions with the grid, as suggested by Jones and Lyon.(112)

In short, TEM studies do not yield reliable information on the apparent size of such weakly-crosslinked, low-monomer concentration particles.
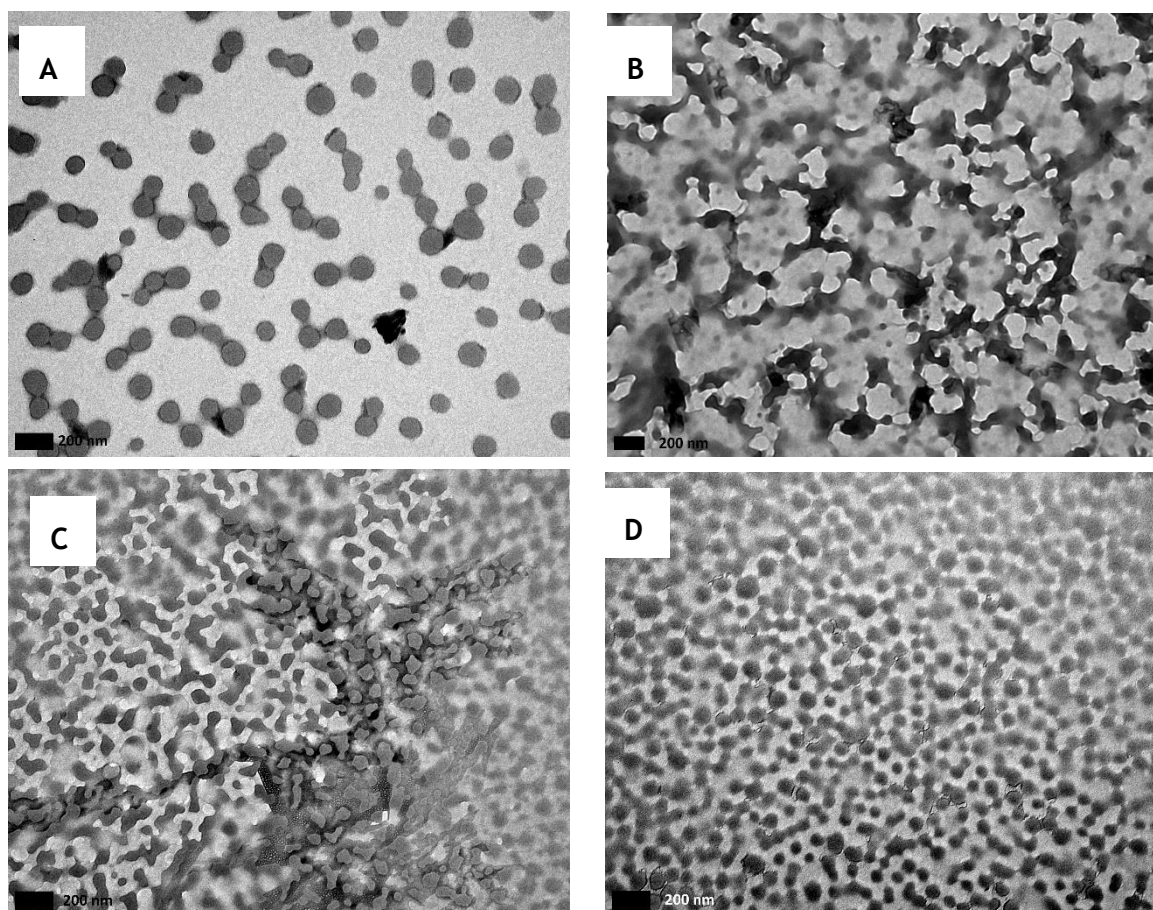
Figure 16. TEM images for PNIPAM (**A**), core (**B**), shell (**C**) and core-shell (**D**) microgels. Scale bars: 200nm. 50000x amplification for all images but B (40000X).

3.3.4. Chemical profile

The chemical composition of polymeric microgels provides information about the success of the polymerization and the presence of contaminants. As such, ATR-FTIR analysis was performed for solutions of PNIPAM, core, shell, and core-shell microgels with different treatments (unwashed, centrifuged, or centrifuged and lyophilized).

According to Fig. 17 (see *Appendix B* for more detail), all spectra comprise peaks at ~3500cm^{-1} corresponding to N-H stretching, ~1640cm^{-1} corresponding to C=O stretching,

and ~1548cm^{-1} corresponding to C-N stretching, all relative to the amide bonds of PNIPAM. The peak at ~3299 cm^{-1} probably corresponds to the O-H stretching of water, and the =C-H stretch peak at ~3050 cm^{-1} possibly corresponds to the unreacted methacrylate and acrylamide groups that were unsuccessfully removed. The -C-H stretching region is located between ~2975 cm^{-1} and ~2875 cm^{-1} and is represented by three peaks. Similarly, the C–H deformation region is also characterized by three peaks at approximately 1460cm^{-1}, 1387cm^{-1} and 1371cm^{-1}.

Tertiary amines do not show peaks relative to N-H stretching, so there is little difference between DMAEMA-containing particles and the remaining samples. PEGMA can be identified through the C-H stretching at ~2875 cm^{-1}, C-O-C stretching at 1250 cm^{-1}, and strong peaks at ~1718cm^{-1} and ~1106 cm^{-1}, corresponding to C=O and C-O stretching, respectively (*see Appendix B*). In this context, the bonds through which PEGMA can be uniquely identified would be at 1250cm^{-1} and ~1106cm^{-1}. While the 1106 cm^{-1} signal can only be visibly observed in shell and unwashed core-shell particles, the 1250cm^{-1} peak is only represented as a very slight depression in the core-shell samples (*see Appendix B*). Having in mind that the amount of PEGMA employed in the synthesis was also very low, no solid conclusions can be taken from FTIR on the presence of PEGMA in the samples, to corroborate the results of the thermo-responsivity studies. To confirm that some PEGMA was incorporated in the sample, protein adsorption tests should be conducted in the future.
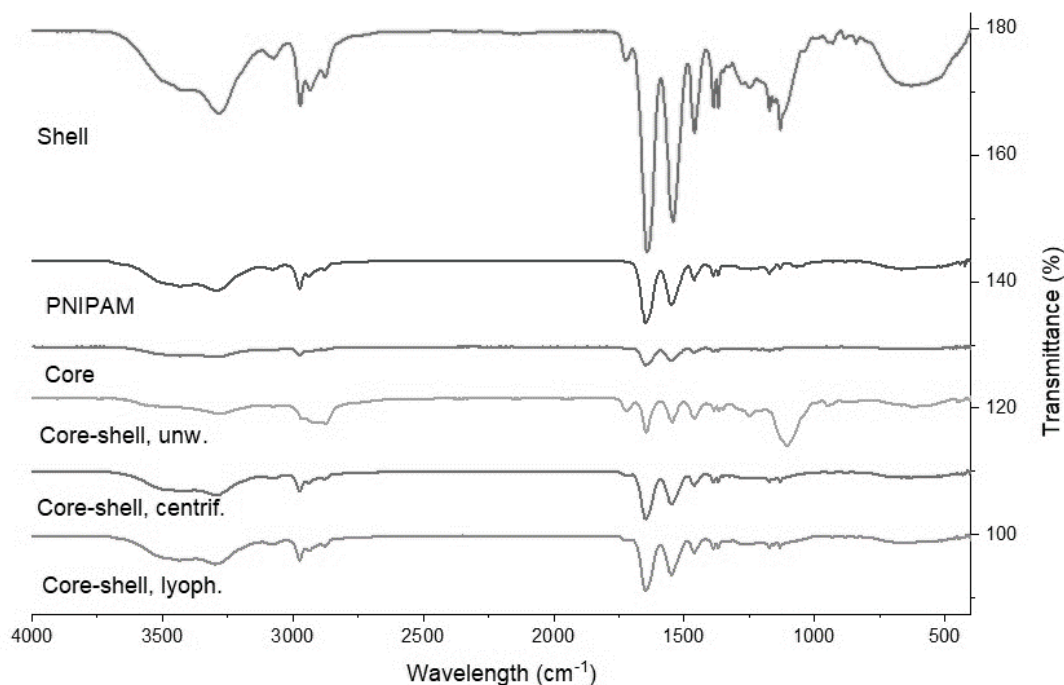
Figure 17. Fourier transformed infrared spectrogram of shell, core-shell (unwashed, centrifuged and lyophilized), core and PNIPAM microgels. Shell, core, and PNIPAM particles were centrifuged prior to this analysis. Curves are represented in order and according to the legend. Vertical offset was adjusted for individual curve analysis. One measurement per sample was performed.

3.4. Encapsulation of ceramic nanorods on polymeric microgels

The purpose of synthesizing both ceramic and polymeric particles would be to integrate the ceramic nano-needles into the core-shell polymeric microgels. With that purpose, two approaches were tested: addition of the ceramics mid-polymerization (mixing method) or coating of the ceramics with the particle (coating method). Both were analysed by TEM to determine the success of the encapsulation.
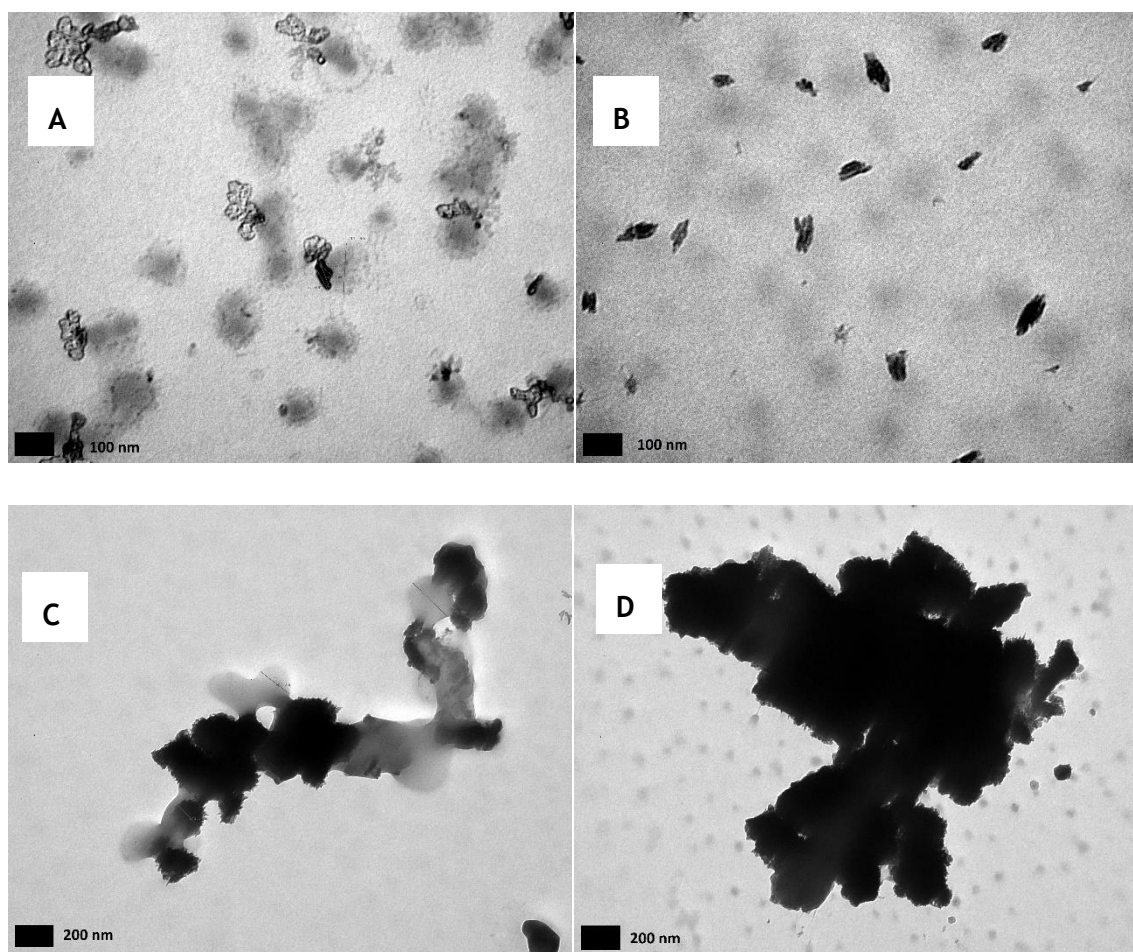
Figure 18. Representative TEM images of the attempts of FeHAP encapsulation onto core-shell microgels through the mixing (**A**) and coating (**B**) methods. *C and D:* TEM images of rare successful encapsulations with the coating method. Notice how ceramic clusters adopted a slightly rounder shape inside the microgel agglomerates.

Electron microscopy images (Fig.18.A,B) proved that the encapsulation was not successful in any of the methods tested. After FTIR analysis of the core-shell microgels, one possible explanation is the fact that the shell formation step of the core-shell

microgels did not occur extensively. Thus, since the encapsulation was performed during that step, not many particles are expected to have been retained in the polymeric matrix. More encapsulation methods could be successful if the ceramics were integrated into the core, into a stronger shell or into the interface of both.

In any case, nano-needle aggregates seem to have been encapsulated in a small number of microgels through the coating methods, although with some signs of rupture.(Fig.18.C,D). This damage may result from a) the vacuum conditions of TEM analysis; b) the existence of excessively large ceramic aggregates; or c) the piercing effect of the nano-needles, which could be smoothened if more spherical ceramics were used. As reported before, TEM preparation most likely inflicts damage to the integrity of the microgels, and so other imaging alternatives should be sought.

3.5. Drug loading on polymeric microgels

After the synthesis, washing and lyophilization of the core-shell microgels, the drug doxorubicin (DOX) was loaded into these particles. To assess the encapsulation efficiency (EE%) and drug loading capacity (LC%), a preliminary test was performed using a gel filtration column with Sephadex® G-25.
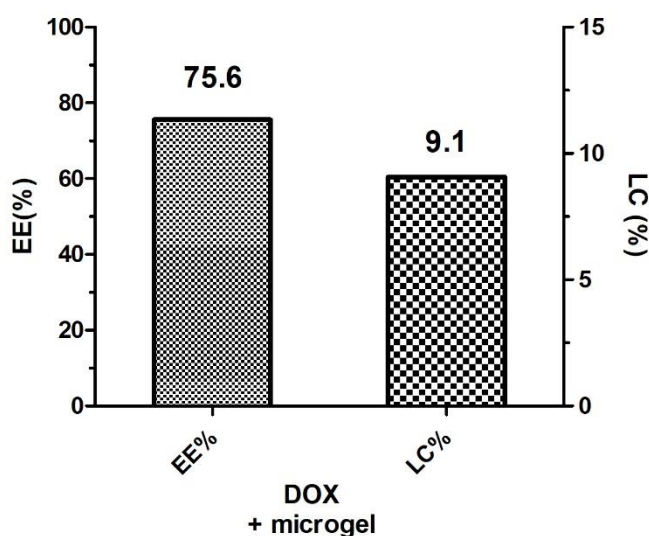
Figure 19. Encapsulation efficiency (EE%) and drug loading capacity (LC%) of DOX loading into core-shell microgels.

Lyophilized microgels (5mg/mL) were suspended in a 0.5mL solution of DOX 0.6mg/mL in PBS and filtered through the 25kDa cut-off gel. Given that the molecular weight of DOX is approximately 500Da, it was expected that the free drug eluted rapidly. Core-shell microgels were not expected to pass the 25kDa filter, since this molecular weight cut-off corresponds to a hydrodynamic pore size of ~2nm.(147) The eluted free

drug was collected and analysed, and yielded a final EE of 75.6% and a LC of 9.1% (Fig.19).

With this, the final EE% and LC% showed satisfactory loading of the hydrophobic drug. Previous works report rather similar results, with DOX loading capacities of up to 8.7% in PEG/Pluronic F-127 carriers(148) and 75% encapsulation efficiency in PLGA nanoparticles(149), although with EE percentages as high as 92% in liposomes.(150) The next step would involve the release of DOX from the microgels in a biologically relevant buffer, such as PBS, at different temperature and pH conditions, in order to recreate the environments of the bloodstream, tumour milieu or inside the endosomes, and evaluate release rates accordingly.

3.6. Cell metabolic activity assays

Fibroblasts are one of the several types of stromal cells that surround cancer tissues. With this in mind, to study the effect of the ethanol-sterilized core-shell microgels on cell viability, human gingival fibroblasts were incubated with these materials at a 5mg/mL concentration and their metabolic activity was evaluated through the resazurin assay at 4h and 24h, as a preliminary test.

Cells incubated with microgels showed an average increase in metabolic activity when compared to the control at both 4h and 24h timepoints (Fig.20). However, due to the considerable technical error associated with the measurements, it cannot be concluded that the microgels increase fibroblast metabolic activity. Instead, it can only be observed that the microgels do not seem to reduce cell viability - still a promising result. Naturally the repetition of this assay should be conducted to further complement this work, not just in fibroblasts but also in triple negative cancer cell lines.
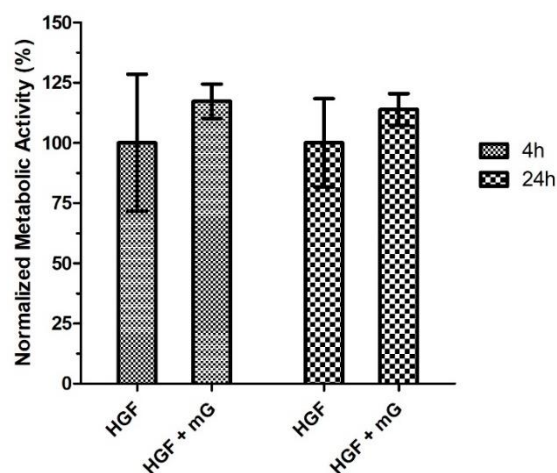
Figure 20. Normalized metabolic activity of human gingival fibroblasts (HGF) after 4h and 24h incubating with core-shell microgels *(mG)*. Data represented as mean ± SD (n=3 measurements, n=1 assay).

MDA-MB-468 is one relevant cell line for the extension of this work, as it is a triple negative breast cancer (TNBC) cell line with amplified EGFR expression. The development of a "smart" microgel capsule that could carry DOX would reduce the side effects of such a difficult therapy, especially if the microgels carried a covalently-linked EGF or an appropriate monoclonal antibody. Future studies may introduce one of these material modifications in order to more specifically target TNBCs.

3.7. Cell morphology

To assess the morphology of the fibroblasts after incubation with the microgels, the cells were stained with DAPI for blue nuclei and Alexa Fluor 488® for green F-actin and seen under an inverted fluorescence microscope.
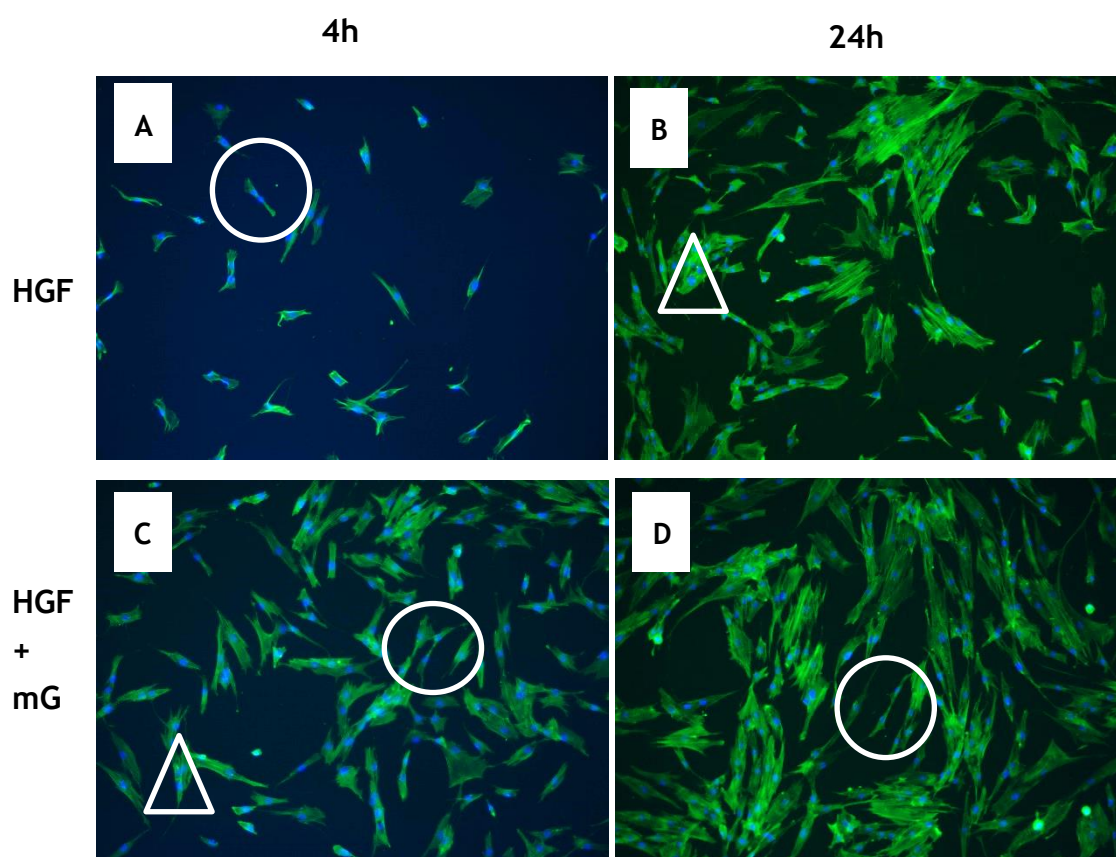
Figure 21. Fluorescent microscope images of human gingival fibroblasts (HGF) non-incubated (**A,B**) and incubated with ethanol-treated microgels (**C,D**), for 4h and 24h. Nuclei were stained with DAPI and F-actin with Alexa Fluor® 488. All images have been equally enhanced for contrast and brightness in agreement with the *Journal of Cell Biology* policies. Triangles and circles indicate cells undergoing mitosis.

The stretched morphology of the adhered fibroblasts was reported in every scenario, with a limited number of non-adhered cells (Fig.21). The cell density of the present images is in agreement with the metabolic activity assay results presented before. Cells undergoing mitosis and at the final stages of mitosis can be seen in every condition and are generally identified by the presence of binucleated cytoplasm areas (indicated by triangles) or two still-connected single-nucleated cells (indicated by circles, Fig.21). The fibroblasts also exhibit long pseudopods, associated with their migrating activity.

In conclusion, cells incubated with microgels showed signs of relatively maintained viability, still dividing and migrating, in agreement with the metabolic activity assay. For future studies, morphology studies could be performed in cancer cell lines or, more interestingly, in co-cultures of cancer cells and fibroblasts.

(page intentionally left blank)

Chapter IV

Conclusions and Perspectives

In this work, the design of a novel, thermo-responsive magnetic nanocomposite comprising FeHAP nano-needles entrapped in a copolymeric core-shell microgel of P(NIPAM-DMAEMA)-P(NIPAM-PEGMA) is proposed as the solution to address some problems arising from chemotherapy side effects and MRI contrast agent toxicity.

Iron-doped HAP nano-needles of less than 100 nm in length and less than 20 nm in width were shown to possess TCP and iron oxide phases, and are also thought to have Fe^{3+} substitutions in the HAP lattice. Tricalcium phosphates allow for a more easily degradable particle, quite an advantage in therapy in the sense that calcium imbalance may trigger apoptosis and iron excess may cause an extensive production of reactive oxygen species. The coexistence of superparamagnetic and ferrimagnetic properties in the same material is thought to arise from the presence of single (magnetic) domain and multidomain magnetite/maghemite and iron-doped HAP. While ferrimagnetism is not ideal for T2-weighted MRI contrasting, its signal is reduced and therefore no significant impact is expected; superparamagnetism prevails.

Tumours are usually at higher temperatures (2-3°C) than other tissues due to uncontrolled cell division and blood affluency. As such, when properly tuned, temperature-responsive nanocarriers can deliver drugs and other agents to the tumour site without the need for external stimuli. The transition temperature was hereby fixed at 38.6°C, at which the temperature of most healthy tissues does not normally reach. Sizes below 200nm and the presence of covalently-linked PEG also contributes to the longer circulation half-life of the delivery system and contributes to larger accumulation at tumour sites otherwise unreachable or unknown. For better targeting of breast carcinomas and their metastases, EGF or patient-tailored monoclonal antibodies could also be covalently-linked to the nanocarrier, resulting in a much more specific delivery.

Following the non-successful attempts to encapsulate the nano-needles onto the shell of the microgels, FeHAP should instead be allocated to the polymeric core, allowing more protection from degradation. Similarly, the relatively neutral charge of PNIPAM contributed to a satisfactory loading efficiency of hydrophobic DOX and its consequent protection from fast clearance. Cell metabolic activity also appeared to be unaffected by bare microgels, hinting at a low cytotoxicity.

In addition to MRI contrasting, magnetic hyperthermia may also be another application of these nano-needles, although more tests should be run. This heating phenomenon is usually mediated by superparamagnetic particles with relatively high M_s values, and the purpose is to heat tissues at a temperature of approximately 42°C for a certain period of time. Now, sintered FeHAP showed superparamagnetism but low M_s values, but if an aqueous suspension of FeHAP proved able to reach a heating plateau at 42°C at a reasonable particle concentration, its potential for this type of treatment would be confirmed.

Along with ferrimagnetism, another possible physical characteristic of iron-based products is ferroelectricity, associated with pyro- and piezoelectricity. Notably, these electric behaviours have been reported in undoped, polar hexagonal HAP.(62) To assess if FeHAP is not just responsive to magnetic fields but also to electricity, future studies could start by assessing the polarity of the sample and, should the results be favourable to a polarized structure, proceed to piezoresponse force microscopy for further characterization. By responding to both stimuli, the nano-needles could thus be easily controlled both internally and externally.

Along with drug and MRI contrast agent loading, the nano-system could also carry important nucleic acids. Gene therapy, currently a hot topic in the scientific community, relies on the efficiency of gene delivery and transfection, and DMAEMA-containing materials have shown outstanding success rates on these aspects. Yet another functionality could be tested without major modifications of the polymer.

To conclude, the market approval of tailored multifunctional nanocarriers could pave the way for the establishment of personalized medicine. The emerging field of theranostics has aimed to gather both therapeutic and diagnostic functionalities in one single system at the nanoscale with the least toxicity, most simplicity, and best cost-effectiveness. The growing interest from the biomedical scientific community has led to an unprecedented number of publications on this field, and it will be not before long that "smart" materials start entering clinical trial and marketing phases, contributing to fast developments in an ever-evolving area.

(page intentionally left blank)

(page intentionally left blank)

References

1.	Centers for Disease Control and Prevention [Available from: https://www.cdc.gov/nchs/fastats/leading-causes-of-death.htm.
2.	World Health Organization [Available from: http://www.who.int/cancer/en/.
3.	Siegel RL, Miller KD, Jemal A. Cancer Statistics, 2017. CA: a cancer journal for clinicians. 2017;67(1):7-30.
4.	Ghoncheh M, Pournamdar Z, Salehiniya H. Incidence and Mortality and Epidemiology of Breast Cancer in the World. Asian Pacific journal of cancer prevention : APJCP. 2016;17(S3):43-6.
5.	Dent R, Trudeau M, Pritchard KI, Hanna WM, Kahn HK, Sawka CA, et al. Triple-Negative Breast Cancer: Clinical Features and Patterns of Recurrence. Clinical Cancer Research. 2007;13(15):4429.
6.	Clark WH. Tumour progression and the nature of cancer. British Journal of Cancer. 1991;64(4):631-44.
7.	Bremnes RM, Dønnem T, Al-Saad S, Al-Shibli K, Andersen S, Sirera R, et al. The Role of Tumor Stroma in Cancer Progression and Prognosis: Emphasis on Carcinoma-Associated Fibroblasts and Non-small Cell Lung Cancer. Journal of Thoracic Oncology. 2011;6(1):209-17.
8.	Sounni NE, Noel A. Targeting the Tumor Microenvironment for Cancer Therapy. Clinical Chemistry. 2013;59(1):85.
9.	Zwicke GL, Mansoori GA, Jeffery CJ. Utilizing the folate receptor for active targeting of cancer nanotherapeutics. Nano Reviews. 2012;3:10.3402/nano.v3i0.18496.
10.	Daniels TR, Bernabeu E, Rodriguez JA, Patel S, Kozman M, Chiappetta DA, et al. The transferrin receptor and the targeted delivery of therapeutic agents against cancer. Biochimica et biophysica acta. 2012;1820(3):291-317.
11.	Desgrosellier JS, Cheresh DA. Integrins in cancer: biological implications and therapeutic opportunities. Nature reviews Cancer. 2010;10(1):9-22.
12.	de Villiers MM, Aramwit P, Kwon GS. Nanotechnology in Drug Delivery: Springer New York; 2008.
13.	Baba AI, Catoi C. Comparative Oncology. Bucharest: The Publishing House of the Romanian Academy
The Publishing House of the Romanian Academy.; 2007.
14.	Lee YT. Breast carcinoma: pattern of metastasis at autopsy. Journal of surgical oncology. 1983;23(3):175-80.
15.	Dasari S, Tchounwou PB. Cisplatin in cancer therapy: molecular mechanisms of action. European journal of pharmacology. 2014;0:364-78.
16.	Thorn CF, Oshiro C, Marsh S, Hernandez-Boussard T, McLeod H, Klein TE, et al. Doxorubicin pathways: pharmacodynamics and adverse effects. Pharmacogenetics and Genomics. 2011;21(7):440-6.
17.	Reed JC. Apoptosis-targeted therapies for cancer. Cancer Cell. 2003;3(1):17-22.
18.	Giorgi C, Baldassari F, Bononi A, Bonora M, De Marchi E, Marchi S, et al. Mitochondrial Ca(2+) and apoptosis. Cell calcium. 2012;52(1):36-43.
19.	Han Y, Li S, Cao X, Yuan L, Wang Y, Yin Y, et al. Different Inhibitory Effect and Mechanism of Hydroxyapatite Nanoparticles on Normal Cells and Cancer Cells In Vitro and In Vivo. Scientific Reports. 2014;4:7134.
20.	Tsurusawa M, Niwa M, Katano N, Fujimoto T. Methotrexate cytotoxicity as related to irreversible S phase arrest in mouse L1210 leukemia cells. Japanese journal of cancer research : Gann. 1990;81(1):85-90.
21.	Waldman T, Zhang Y, Dillehay L, Yu J, Kinzler K, Vogelstein B, et al. Cell-cycle arrest versus cell death in cancer therapy. Nature medicine. 1997;3(9):1034-6.
22.	American Cancer Society. [Available from: https://www.cancer.org/treatment/understanding-your-diagnosis/tests/imaging-radiology-tests-for-cancer.html.

23.   Vadivambal R, Jayas DS. Bio-Imaging: Principles, Techniques, and Applications: Taylor & Francis; 2015.
24.   Stark DD, Bradley WG. Magnetic Resonance Imaging: Brain, head and neck, spine: Mosby; 1999.
25.   Mitchell DG, Cohen M. MRI Principles: Saunders; 2004.
26.   Urruticoechea A, Alemany R, Balart J, Villanueva A, Vinals F, Capella G. Recent advances in cancer therapy: an overview. Current pharmaceutical design. 2010;16(1):3-10.
27.   Chabner BA, Roberts TG, Jr. Timeline: Chemotherapy and the war on cancer. Nat Rev Cancer. 2005;5(1):65-72.
28.   Zhang Z, Mei L, Feng SS. Paclitaxel drug delivery systems. Expert opinion on drug delivery. 2013;10(3):325-40.
29.   Dang W, Colvin OM, Brem H, Saltzman WM. Covalent coupling of methotrexate to dextran enhances the penetration of cytotoxicity into a tissue-like matrix. Cancer research. 1994;54(7):1729-35.
30.   Dheer D, Arora D, Jaglan S, Rawal RK, Shankar R. Polysaccharides based nanomaterials for targeted anti-cancer drug delivery. Journal of drug targeting. 2017;25(1):1-16.
31.   Venkatesan J, Lee JY, Kang DS, Anil S, Kim SK, Shim MS, et al. Antimicrobial and anticancer activities of porous chitosan-alginate biosynthesized silver nanoparticles. International journal of biological macromolecules. 2017;98:515-25.
32.   Manatunga DC, de Silva RM, de Silva KMN, de Silva N, Bhandari S, Yap YK, et al. pH responsive controlled release of anti-cancer hydrophobic drugs from sodium alginate and hydroxyapatite bi-coated iron oxide nanoparticles. European journal of pharmaceutics and biopharmaceutics : official journal of Arbeitsgemeinschaft fur Pharmazeutische Verfahrenstechnik eV. 2017;117:29-38.
33.   He Q, Shi J, Chen F, Zhu M, Zhang L. An anticancer drug delivery system based on surfactant-templated mesoporous silica nanoparticles. Biomaterials. 2010;31(12):3335-46.
34.   Weerasuriya DRK, Wijesinghe W, Rajapakse RMG. Encapsulation of anticancer drug copper bis(8-hydroxyquinoline) in hydroxyapatite for pH-sensitive targeted delivery and slow release. Materials science & engineering C, Materials for biological applications. 2017;71:206-13.
35.   Gotman I, Psakhie SG, Lozhkomoev AS, Gutmanas EY. Iron oxide and gold nanoparticles in cancer therapy. AIP Conference Proceedings. 2016;1760(1):020020.
36.   Baselga J, Tripathy D, Mendelsohn J, Baughman S, Benz CC, Dantis L, et al. Phase II study of weekly intravenous recombinant humanized anti-p185HER2 monoclonal antibody in patients with HER2/neu-overexpressing metastatic breast cancer. Journal of clinical oncology : official journal of the American Society of Clinical Oncology. 1996;14(3):737-44.
37.   Medina PJ, Goodin S. Lapatinib: a dual inhibitor of human epidermal growth factor receptor tyrosine kinases. Clinical therapeutics. 2008;30(8):1426-47.
38.   Jordan VC. Tamoxifen (ICI46,474) as a targeted therapy to treat and prevent breast cancer. British Journal of Pharmacology. 2006;147(Suppl 1):S269-S76.
39.   Johannessen DC, Engan T, Di Salle E, Zurlo MG, Paolini J, Ornati G, et al. Endocrine and clinical effects of exemestane (PNU 155971), a novel steroidal aromatase inhibitor, in postmenopausal breast cancer patients: a phase I study. Clinical cancer research : an official journal of the American Association for Cancer Research. 1997;3(7):1101-8.
40.   Miele E, Spinelli GP, Miele E, Tomao F, Tomao S. Albumin-bound formulation of paclitaxel (Abraxane(®) ABI-007) in the treatment of breast cancer. International Journal of Nanomedicine. 2009;4:99-105.
41.   Yuan D-m, Lv Y-l, Yao Y-w, Miao X-h, Wang Q, Xiao X-w, et al. Efficacy and safety of Abraxane in treatment of progressive and recurrent non-small cell lung cancer patients: A retrospective clinical study. Thoracic Cancer. 2012;3(4):341-7.
42.   Perez AT, Domenech GH, Frankel C, Vogel CL. Pegylated liposomal doxorubicin (Doxil) for metastatic breast cancer: the Cancer Research Network, Inc., experience. Cancer investigation. 2002;20 Suppl 2:22-9.
43.   Johnston SR, Gore ME. Caelyx: phase II studies in ovarian cancer. European journal of cancer (Oxford, England : 1990). 2001;37 Suppl 9:S8-14.
44.   Rom J, Bechstein S, Domschke C, Golatta M, Mayer C, Heil J, et al. Efficacy and toxicity profile of pegylated liposomal doxorubicin (Caelyx) in patients with advanced breast cancer. Anti-cancer drugs. 2014;25(2):219-24.

45.   Vert M, Doi Y, Hellwich K-H, Hess M, Hodge P, Kubisa P, et al. Terminology for biorelated polymers and applications (IUPAC Recommendations 2012). Pure and Applied Chemistry2012. p. 377.

46.   International Organization for Standardization [Available from: http://www.iso.org/iso/iso_catalogue.htm.

47.   Burgess DJ, Duffy E, Etzler F, Hickey AJ. Particle size analysis: AAPS workshop report, cosponsored by the Food and Drug Administration and the United States Pharmacopeia. The AAPS journal. 2004;6(3):e20.

48.   Salata OV. Applications of nanoparticles in biology and medicine. Journal of Nanobiotechnology. 2004;2:3-.

49.   Bobo D, Robinson KJ, Islam J, Thurecht KJ, Corrie SR. Nanoparticle-Based Medicines: A Review of FDA-Approved Materials and Clinical Trials to Date. Pharmaceutical research. 2016;33(10):2373-87.

50.   Cacheris WP, Quay SC, Rocklage SM. The relationship between thermodynamics and the toxicity of gadolinium complexes. Magnetic resonance imaging. 1990;8(4):467-81.

51.   Swaminathan S. Gadolinium toxicity: Iron and ferroportin as central targets. Magnetic resonance imaging. 2016;34(10):1373-6.

52.   Burke LM, Ramalho M, AlObaidy M, Chang E, Jay M, Semelka RC. Self-reported gadolinium toxicity: A survey of patients with chronic symptoms. Magnetic resonance imaging. 2016;34(8):1078-80.

53.   Hentze MW, Muckenthaler MU, Andrews NC. Balancing acts: molecular control of mammalian iron metabolism. Cell. 2004;117(3):285-97.

54.   Idee J-M, Port M, Raynal I, Schaefer M, Bonnemain B, Prigent P, et al. Superparamagnetic Nanoparticles of Iron Oxides for Magnetic Resonance Imaging Applications. Nanotechnologies for the Life Sciences: Wiley-VCH Verlag GmbH & Co. KGaA; 2007.

55.   Fortuin AS, Brüggemann R, van der Linden J, Panfilov I, Israël B, Scheenen TWJ, et al. Ultra-small superparamagnetic iron oxides for metastatic lymph node detection: back on the block. Wiley Interdisciplinary Reviews: Nanomedicine and Nanobiotechnology. 2018;10(1):e1471-n/a.

56.   Barrow M, Taylor A, Fuentes-Caparrós AM, Sharkey J, Daniels LM, Mandal P, et al. SPIONs for cell labelling and tracking using MRI: magnetite or maghemite? †Electronic supplementary information (ESI) available: pXRD, DLS, zeta potential, TEM, TGA, MRI and XANES. See DOI: 10.1039/c7bm00515f. Biomaterials science. 2018;6(1):101-6.

57.   Tampieri A, D'Alessandro T, Sandri M, Sprio S, Landi E, Bertinetti L, et al. Intrinsic magnetism and hyperthermia in bioactive Fe-doped hydroxyapatite. Acta biomaterialia. 2012;8(2):843-51.

58.   Gloria A, Russo T, D'Amora U, Zeppetelli S, D'Alessandro T, Sandri M, et al. Magnetic poly(ε-caprolactone)/iron-doped hydroxyapatite nanocomposite substrates for advanced bone tissue engineering. Journal of The Royal Society Interface. 2013;10(80).

59.   Laranjeira MS, Moço A, Ferreira J, Coimbra S, Costa E, Santos-Silva A, et al. Different hydroxyapatite magnetic nanoparticles for medical imaging: Its effects on hemostatic, hemolytic activity and cellular cytotoxicity. Colloids and Surfaces B: Biointerfaces. 2016;146:363-74.

60.   Lopes JR, Santos G, Barata P, Oliveira R, Lopes CM. Physical and chemical stimuli-responsive drug delivery systems: targeted delivery and main routes of administration. Current pharmaceutical design. 2013;19(41):7169-84.

61.   Dinger SC, Fridjhon P, Rubin DM. Thermal Excitation of Gadolinium-Based Contrast Agents Using Spin Resonance. PLOS ONE. 2016;11(6):e0158194.

62.   Haverty D, Tofail SAM, Stanton KT, McMonagle JB. Structure and stability of hydroxyapatite: Density functional calculation and Rietveld analysis. Physical Review B. 2005;71(9):094103.

63.   Lang SB, Tofail SAM, Kholkin AL, Wojtaś M, Gregor M, Gandhi AA, et al. Ferroelectric Polarization in Nanocrystalline Hydroxyapatite Thin Films on Silicon. Scientific Reports. 2013;3:2215.

64.   Tofail S, Joanna B. Electrically Active Materials For Medical Devices: World Scientific Publishing Company; 2016.

65.   Zhang Y, Chen L, Zeng J, Zhou K, Zhang D. Aligned porous barium titanate/hydroxyapatite composites with high piezoelectric coefficients for bone tissue

engineering. Materials science & engineering C, Materials for biological applications. 2014;39:143-9.

66. Yang Z, Zhang C. Molecularly imprinted hydroxyapatite thin film for bilirubin recognition. Biosensors & bioelectronics. 2011;29(1):167-71.

67. Ding Y, Liu J, Wang H, Shen G, Yu R. A piezoelectric immunosensor for the detection of alpha-fetoprotein using an interface of gold/hydroxyapatite hybrid nanomaterial. Biomaterials. 2007;28(12):2147-54.

68. Ding Y, Liu J, Jin X, Lu H, Shen G, Yu R. Poly-L-lysine/hydroxyapatite/carbon nanotube hybrid nanocomposite applied for piezoelectric immunoassay of carbohydrate antigen 19-9. The Analyst. 2008;133(2):184-90.

69. Zhang Y, Wang H, Yan B, Zhang Y, Li J, Shen G, et al. A reusable piezoelectric immunosensor using antibody-adsorbed magnetic nanocomposite. Journal of immunological methods. 2008;332(1-2):103-11.

70. Li Z, Ye E, David, Lakshminarayanan R, Loh XJ. Recent Advances of Using Hybrid Nanocarriers in Remotely Controlled Therapeutic Delivery. Small (Weinheim an der Bergstrasse, Germany). 2016;12(35):4782-806.

71. Lawson RN, Chughtai MS. Breast Cancer and Body Temperature. Canadian Medical Association Journal. 1963;88(2):68-70.

72. Babincova M, Cicmanec P, Altanerova V, Altaner C, Babinec P. AC-magnetic field controlled drug release from magnetoliposomes: design of a method for site-specific chemotherapy. Bioelectrochemistry (Amsterdam, Netherlands). 2002;55(1-2):17-9.

73. Hu SH, Tsai CH, Liao CF, Liu DM, Chen SY. Controlled rupture of magnetic polyelectrolyte microcapsules for drug delivery. Langmuir : the ACS journal of surfaces and colloids. 2008;24(20):11811-8.

74. Sutani K, Kaetsu I, Uchida K. The synthesis and the electric-responsiveness of hydrogel entrapping natural polyelectrolyte2001. 49-54 p.

75. Junwu K, Zhigang Y, Taijiang P, Guangming C, Boda W. Design and test of a high-performance piezoelectric micropump for drug delivery. Sensors and Actuators A: Physical. 2005;121(1):156-61.

76. Ehrenberg O, Kósa G, editors. Analysis of a novel piezoelectric micro-pump for drug delivery in a medical integrated micro system. 2012 4th IEEE RAS & EMBS International Conference on Biomedical Robotics and Biomechatronics (BioRob); 2012 24-27 June 2012.

77. Atul ST, Babu MCL, editors. Characterization of valveless micropump for drug delivery by using piezoelectric effect. 2016 International Conference on Advances in Computing, Communications and Informatics (ICACCI); 2016 21-24 Sept. 2016.

78. Niu K, Yao Y, Xiu M, Guo C, Ge Y, Wang J. Controlled Drug Delivery by Polylactide Stereocomplex Micelle for Cervical Cancer Chemotherapy. Frontiers in pharmacology. 2018;9:930.

79. Cao J, Chen D, Huang S, Deng D, Tang L, Gu Y. Multifunctional near-infrared light-triggered biodegradable micelles for chemo- and photo-thermal combination therapy. Oncotarget. 2016;7(50):82170-84.

80. Popescu I, Prisacaru AI, Suflet DM, Fundueanu G. Thermo- and pH-sensitivity of poly(N-vinylcaprolactam-co-maleic acid) in aqueous solution. Polymer Bulletin. 2014;71(11):2863-80.

81. Shakoori Z, Ghanbari H, Omidi Y, Pashaiasl M, Akbarzadeh A, Jomeh Farsangi Z, et al. Fluorescent multi-responsive cross-linked P(N-isopropylacrylamide)-based nanocomposites for cisplatin delivery. Drug development and industrial pharmacy. 2017;43(8):1283-91.

82. van Elk M, van den Dikkenberg JB, Storm G, Hennink WE, Vermonden T, Heger M. Preclinical evaluation of thermosensitive poly(N-(2-hydroxypropyl) methacrylamide mono/dilactate)-grafted liposomes for cancer thermochemotherapy. International journal of pharmaceutics. 2018;550(1-2):190-9.

83. Awino JK, Gudipati S, Hartmann AK, Santiana JJ, Cairns-Gibson DF, Gomez N, et al. Nucleic Acid Nanocapsules for Enzyme-Triggered Drug Release. Journal of the American Chemical Society. 2017;139(18):6278-81.

84. Hirn S, Semmler-Behnke M, Schleh C, Wenk A, Lipka J, Schaffler M, et al. Particle size-dependent and surface charge-dependent biodistribution of gold nanoparticles after intravenous administration. European journal of pharmaceutics and biopharmaceutics : official journal of Arbeitsgemeinschaft fur Pharmazeutische Verfahrenstechnik eV. 2011;77(3):407-16.

85.   Zhang X, Lin Y, Gillies RJ. Tumor pH and its measurement. Journal of nuclear medicine : official publication, Society of Nuclear Medicine. 2010;51(8):1167-70.

86.   Marieb EN. Essentials of Human Anatomy and Physiology Lab Manual: Pearson/Benjamin Cummings; 2005.

87.   Geisow MJ, Evans WH. pH in the endosome. Measurements during pinocytosis and receptor-mediated endocytosis. Experimental cell research. 1984;150(1):36-46.

88.   Schmaljohann D. Thermo- and pH-responsive polymers in drug delivery. Advanced Drug Delivery Reviews. 2006;58(15):1655-70.

89.   Thakral S, Thakral NK, Majumdar DK. Eudragit: a technology evaluation. Expert opinion on drug delivery. 2013;10(1):131-49.

90.   Wei G, Ma PX. Structure and properties of nano-hydroxyapatite/polymer composite scaffolds for bone tissue engineering. Biomaterials. 2004;25(19):4749-57.

91.   Family R, Solati-Hashjin M, Namjoy Nik S, Nemati A. Surface modification for titanium implants by hydroxyapatite nanocomposite. Caspian Journal of Internal Medicine. 2012;3(3):460-5.

92.   Fihri A, Len C, Varma RS, Solhy A. Hydroxyapatite: A review of syntheses, structure and applications in heterogeneous catalysis. Coordination Chemistry Reviews. 2017;347:48-76.

93.   Adibkia K. Application of Hydroxyapatite Nanoparticle in the Drug Delivery Systems2015.

94.   Pepla E, Besharat LK, Palaia G, Tenore G, Migliau G. Nano-hydroxyapatite and its applications in preventive, restorative and regenerative dentistry: a review of literature. Annali di Stomatologia. 2014;5(3):108-14.

95.   Bastami F, Paknejad Z, Jafari M, Salehi M, Rezai Rad M, Khojasteh A. Fabrication of a three-dimensional beta-tricalcium-phosphate/gelatin containing chitosan-based nanoparticles for sustained release of bone morphogenetic protein-2: Implication for bone tissue engineering. Materials science & engineering C, Materials for biological applications. 2017;72:481-91.

96.   Liu X, Zhang Y, Xiong K, Yan M. Fabrication of a Novel Beta Tricalcium Phosphate/Sodium Alginate/Poly(D,L-lactic acid) Composite Microsphere and Its Drug Releasing Property. Journal of nanoscience and nanotechnology. 2018;18(6):3844-9.

97.   Seidenstuecker M, Ruehe J, Suedkamp NP, Serr A, Wittmer A, Bohner M, et al. Composite material consisting of microporous beta-TCP ceramic and alginate for delayed release of antibiotics. Acta biomaterialia. 2017;51:433-46.

98.   Das D, Bang S, Zhang S, Noh I. Bioactive Molecules Release and Cellular Responses of Alginate-Tricalcium Phosphate Particles Hybrid Gel. Nanomaterials (Basel, Switzerland). 2017;7(11).

99.   Ferraz MP, Monteiro FJ, Manuel CM. Hydroxyapatite nanoparticles: A review of preparation methodologies. Journal of applied biomaterials & biomechanics : JABB. 2004;2(2):74-80.

100.   Mateus AY, Barrias CC, Ribeiro C, Ferraz MP, Monteiro FJ. Comparative study of nanohydroxyapatite microspheres for medical applications. Journal of biomedical materials research Part A. 2008;86(2):483-93.

101.   Sooksaen P, Jumpanoi N, Suttiphan P, Kimchaiyong E. Crystallization of Nano-Sized Hydroxyapatite via Wet Chemical Process under Strong Alkaline Conditions. Science Journal Ubon Ratchathani University. 2010.

102.   Kumar R, Prakash KH, Cheang P, Khor KA. Temperature Driven Morphological Changes of Chemically Precipitated Hydroxyapatite Nanoparticles. Langmuir : the ACS journal of surfaces and colloids. 2004;20(13):5196-200.

103.   Ashokan A, Menon D, Nair S, Koyakutty M. A molecular receptor targeted, hydroxyapatite nanocrystal based multi-modal contrast agent. Biomaterials. 2010;31(9):2606-16.

104.   Chandra VS, Baskar G, Suganthi RV, Elayaraja K, Joshy MI, Beaula WS, et al. Blood compatibility of iron-doped nanosize hydroxyapatite and its drug release. ACS applied materials & interfaces. 2012;4(3):1200-10.

105.   Gong C, Qi T, Wei X, Qu Y, Wu Q, Luo F, et al. Thermosensitive polymeric hydrogels as drug delivery systems. Current medicinal chemistry. 2013;20(1):79-94.

106.   Farshbaf M, Salehi R, Annabi N, Khalilov R, Akbarzadeh A, Davaran S. pH- and thermo-sensitive MTX-loaded magnetic nanocomposites: synthesis, characterization, and in vitro studies

on A549 lung cancer cell and MR imaging. Drug development and industrial pharmacy. 2018;44(3):452-62.

107.   Motaali S, Pashaeiasl M, Akbarzadeh A, Davaran S. Synthesis and characterization of smart N-isopropylacrylamide-based magnetic nanocomposites containing doxorubicin anti-cancer drug. Artificial cells, nanomedicine, and biotechnology. 2017;45(3):560-7.

108.   Agarwal S, Zhang Y, Maji S, Greiner A. PDMAEMA based gene delivery materials. Materials Today. 2012;15(9):388-93.

109.   Loh XJ, Ong SJ, Tung YT, Choo HT. Co-delivery of drug and DNA from cationic dual-responsive micelles derived from poly(DMAEMA-co-PPGMA). Materials Science and Engineering: C. 2013;33(8):4545-50.

110.   Cheng H, Wu Z, Wu C, Wang X, Liow SS, Li Z, et al. Overcoming STC2 mediated drug resistance through drug and gene co-delivery by PHB-PDMAEMA cationic polyester in liver cancer cells. Materials science & engineering C, Materials for biological applications. 2018;83:210-7.

111.   Wang X, Liow SS, Wu Q, Li C, Owh C, Li Z, et al. Codelivery for Paclitaxel and Bcl-2 Conversion Gene by PHB-PDMAEMA Amphiphilic Cationic Copolymer for Effective Drug Resistant Cancer Therapy. Macromolecular bioscience. 2017;17(11).

112.   Jones CD, Lyon LA. Synthesis and Characterization of Multiresponsive Core–Shell Microgels. Macromolecules. 2000;33(22):8301-6.

113.   Knop K, Pretzel D, Urbanek A, Rudolph T, Scharf DH, Schallon A, et al. Star-shaped drug carriers for doxorubicin with POEGMA and POEtOxMA brush-like shells: a structural, physical, and biological comparison. Biomacromolecules. 2013;14(8):2536-48.

114.   Turecek PL, Bossard MJ, Schoetens F, Ivens IA. PEGylation of Biopharmaceuticals: A Review of Chemistry and Nonclinical Safety Information of Approved Drugs. Journal of Pharmaceutical Sciences. 2016;105(2):460-75.

115.   Bardal SK, Waechter JE, Martin DS. Chapter 2 - Pharmacokinetics. Applied Pharmacology. Philadelphia: Content Repository Only!; 2011. p. 17-34.

116.   Li SD, Huang L. Pharmacokinetics and biodistribution of nanoparticles. Molecular pharmaceutics. 2008;5(4):496-504.

117.   Wei A, Mehtala JG, Patri AK. Challenges and opportunities in the advancement of nanomedicines. Journal of controlled release : official journal of the Controlled Release Society. 2012;164(2):236-46.

118.   Lin L, Yee SW, Kim RB, Giacomini KM. SLC Transporters as Therapeutic Targets: Emerging Opportunities. Nature reviews Drug discovery. 2015;14(8):543-60.

119.   Lin JH, Yamazaki M. Role of P-glycoprotein in pharmacokinetics: clinical implications. Clinical pharmacokinetics. 2003;42(1):59-98.

120.   Choi HS, Liu W, Misra P, Tanaka E, Zimmer JP, Itty Ipe B, et al. Renal clearance of quantum dots. Nature biotechnology. 2007;25(10):1165-70.

121.   Dobrovolskaia MA, McNeil SE. Handbook of Immunological Properties of Engineered Nanomaterials: World Scientific; 2013.

122.   Wei A, Mehtala JG, Patri AK. Challenges and opportunities in the advancement of nanomedicines. Journal of Controlled Release. 2012;164(2):236-46.

123.   Lv H, Zhang S, Wang B, Cui S, Yan J. Toxicity of cationic lipids and cationic polymers in gene delivery. Journal of Controlled Release. 2006;114(1):100-9.

124.   Kang H, Mintri S, Menon AV, Lee HY, Choi HS, Kim J. Pharmacokinetics, Pharmacodynamics and Toxicology of Theranostic Nanoparticles. Nanoscale. 2015;7(45):18848-62.

125.   Mishra P, Nayak B, Dey RK. PEGylation in anti-cancer therapy: An overview. Asian Journal of Pharmaceutical Sciences. 2016;11(3):337-48.

126.   Schild HG. Poly(N-isopropylacrylamide): experiment, theory and application. Progress in Polymer Science. 1992;17(2):163-249.

127.   Gan D, Lyon LA. Synthesis and Protein Adsorption Resistance of PEG-Modified Poly(N-isopropylacrylamide) Core/Shell Microgels. Macromolecules. 2002;35(26):9634-9.

128.   U. PKS. Combined assays for lactose and galactose by enzymatic reactions. Kieler Milchw Forsch 1929(1929;8:551.).

129.   ThermoFisher. alamarBlue® Cell Viability Assay Protocol [Available from: https://www.thermofisher.com/pt/en/home/references/protocols/cell-and-tissue-analysis/cell-profilteration-assay-protocols/cell-viability-with-alamarblue.html.

130.	Coelho JM, Moreira JA, Almeida A, Monteiro FJ. Synthesis and characterization of HAp nanorods from a cationic surfactant template method. Journal of Materials Science: Materials in Medicine. 2010;21(9):2543-9.
131.	DeBrosse MC, Comfort KK, Untener EA, Comfort DA, Hussain SM. High aspect ratio gold nanorods displayed augmented cellular internalization and surface chemistry mediated cytotoxicity. Materials science & engineering C, Materials for biological applications. 2013;33(7):4094-100.
132.	Young A, Smistad G, Karlsen J, Rolla G, Rykke M. Zeta potentials of human enamel and hydroxyapatite as measured by the Coulter DELSA 440. Advances in dental research. 1997;11(4):560-5.
133.	Wu F, Lin DDW, Chang JH, Fischbach C, Estroff LA, Gourdon D. Effect of the Materials Properties of Hydroxyapatite Nanoparticles on Fibronectin Deposition and Conformation. Crystal Growth & Design. 2015;15(5):2452-60.
134.	Zhang C-Y, Sun X-Y, Ouyang J-M, Gui B-S. Diethyl citrate and sodium citrate reduce the cytotoxic effects of nanosized hydroxyapatite crystals on mouse vascular smooth muscle cells. International Journal of Nanomedicine. 2017;12:8511-25.
135.	Penel G, Leroy G, Rey C, Bres E. MicroRaman spectral study of the PO4 and CO3 vibrational modes in synthetic and biological apatites. Calcified tissue international. 1998;63(6):475-81.
136.	de Faria DLA, Venâncio Silva S, de Oliveira MT. Raman microspectroscopy of some iron oxides and oxyhydroxides. Journal of Raman Spectroscopy. 1997;28(11):873-8.
137.	Hanesch M. Raman spectroscopy of iron oxides and (oxy)hydroxides at low laser power and possible applications in environmental magnetic studies. Geophysical Journal International. 2009;177(3):941-8.
138.	Ru, #xed, z-Baltazar A, Esparza R, Rosas G, #xe9, et al. Effect of the Surfactant on the Growth and Oxidation of Iron Nanoparticles. Journal of Nanomaterials. 2015;2015:8.
139.	Carrodeguas RG, De Aza S. α-Tricalcium phosphate: Synthesis, properties and biomedical applications. Acta biomaterialia. 2011;7(10):3536-46.
140.	Wahajuddin, Arora S. Superparamagnetic iron oxide nanoparticles: magnetic nanoplatforms as drug carriers. International Journal of Nanomedicine. 2012;7:3445-71.
141.	Milichovsky M. Water¡ªA Key Substance to Comprehension of Stimuli-Responsive Hydrated Reticular Systems. Journal of Biomaterials and Nanobiotechnology. 2010;Vol.01No.01:14.
142.	Wu C, Zhou S. Effects of surfactants on the phase transition of poly(N-isopropylacrylamide) in water. Journal of Polymer Science Part B: Polymer Physics. 1996;34(9):1597-604.
143.	Utashiro Y, Takiguchi M, Satoh M. Zeta potential of PNIPAM microgel particles dispersed in water—effects of charged radical initiators vs. OH– ion adsorption. Colloid and Polymer Science. 2017;295(1):45-52.
144.	Hu X, Tong Z, Lyon LA. Control of Poly(N-isopropylacrylamide) Microgel Network Structure by Precipitation Polymerization near the Lower Critical Solution Temperature. Langmuir : the ACS journal of surfaces and colloids. 2011;27(7):4142-8.
145.	Tauer K, Gau D, Schulze S, Völkel A, Dimova R. Thermal property changes of poly(N-isopropylacrylamide) microgel particles and block copolymers. Colloid and Polymer Science. 2009;287(3):299.
146.	Jalili NA, Jaiswal MK, Peak CW, Cross LM, Gaharwar AK. Injectable nanoengineered stimuli-responsive hydrogels for on-demand and localized therapeutic delivery. Nanoscale. 2017;9(40):15379-89.
147.	Erickson HP. Size and Shape of Protein Molecules at the Nanometer Level Determined by Sedimentation, Gel Filtration, and Electron Microscopy. Biological Procedures Online. 2009;11:32-51.
148.	Missirlis D, Kawamura R, Tirelli N, Hubbell JA. Doxorubicin encapsulation and diffusional release from stable, polymeric, hydrogel nanoparticles. European journal of pharmaceutical sciences : official journal of the European Federation for Pharmaceutical Sciences. 2006;29(2):120-9.
149.	Lakshmi Priya Krishnamoorthy RKM, Devan Umapathy, Mahesh Kumar, Kannan NG, Antony Joseph Velanganni Arockiam. Encapsulation of Doxorubicin in PLGA Nanoparticles Enhances Cancer Therapy. Clinics in Oncology. 2017(2):1325.

150.   Alyane M, Barratt G, Lahouel M. Remote loading of doxorubicin into liposomes by transmembrane pH gradient to reduce toxicity toward H9c2 cells. Saudi Pharmaceutical Journal. 2016;24(2):165-75.

Appendix

Appendix A

A.1. Hydroxyapatite stabilization with different sodium citrate-to-iron-doped hydroxyapatite (NaCit:FeHAP) ratios

Table A. 1. Hydrodynamic size and surface charge measurements by dynamic light scattering (DLS) of iron-doped hydroxyapatite (FeHAP) stabilized with sodium citrate (NaCit) at weight ratios of 0.5, 1 and 2. Data represented as mean ± SD (n=3 measurements, n=1 assay).

Sample	PdI	Z-average (nm)	Main Intensity Peak (nm)	Zeta Potential (mV)
NaCit:FeHAP 0.5	0.231 ± 0.011	178.9 ± 0.83	208.0 ± 15.6	-42.1 ± 4.77
NaCit:FeHAP 1	0.161 ± 0.015	168.4 ± 3.15	203.5 ± 8.3	-41.2 ± 1.27
NaCit:FeHAP 2	0.218 ± 0.019	171.6 ± 2.24	214.3 ± 17.96	-43.3 ± 2.31

Figure A. 1. Iron-doped hydroxyapatite (FeHAP) stabilized with sodium citrate (NaCit). From left to right: NaCit:FeHAP ratios of 2, 1 and 0.5. While the rightmost sample produced the best stabilization results by DLS, it showed clear deposition over 24h. The most successful stabilizer ratio is, therefore, the one correspondent to the middle sample (NaCit:FeHAP 1).

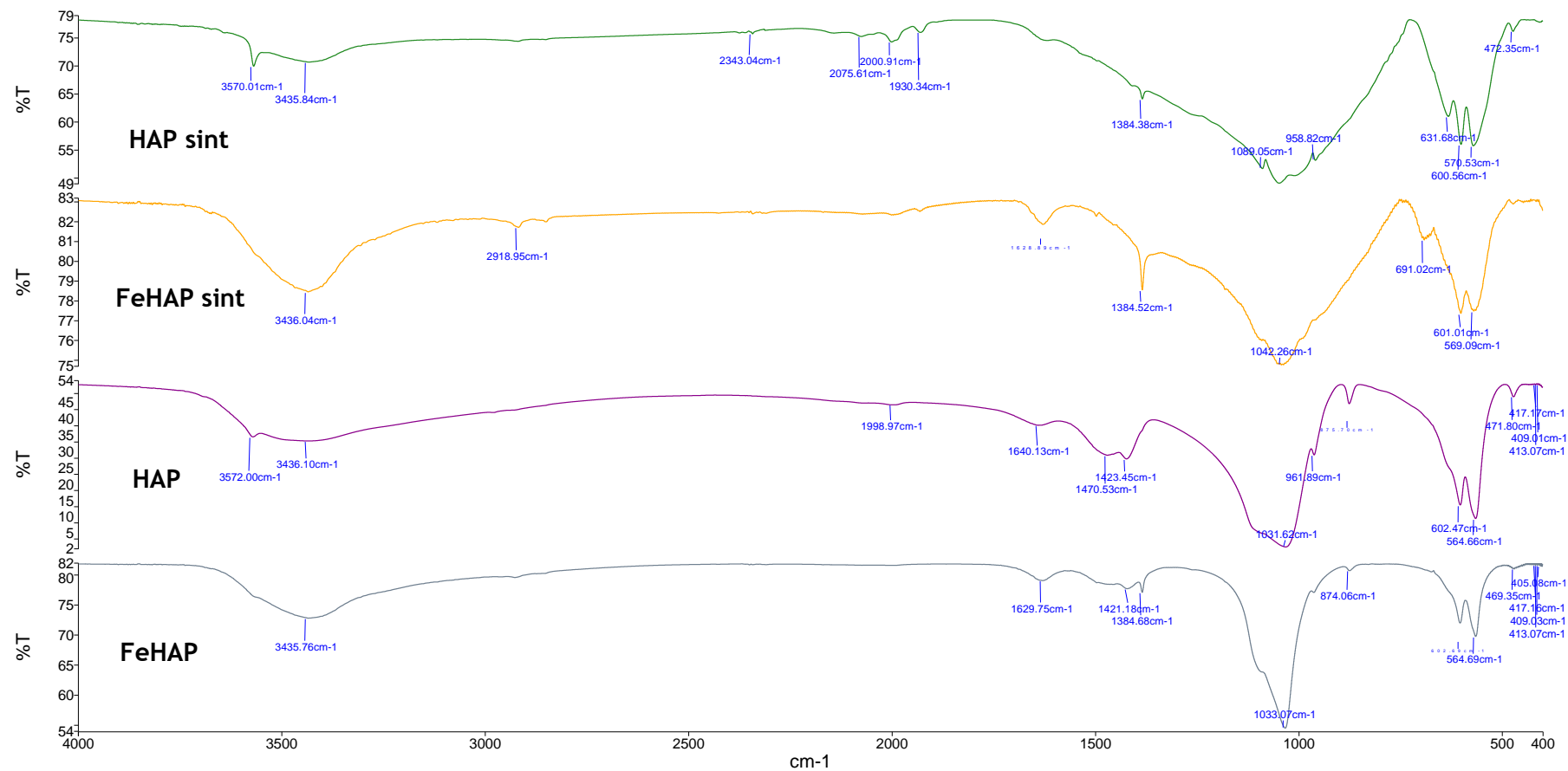## A.2. FTIR spectra of sintered and non-sintered HAP and FeHAP

Figure A. 2. Fourier transform infrared spectra of sintered (*sint*) and non-sintered hydroxyapatite (HAP) and iron-doped hydroxyapatite (FeHAP). Vertical offset was adjusted for individual curve analysis.

Appendix B

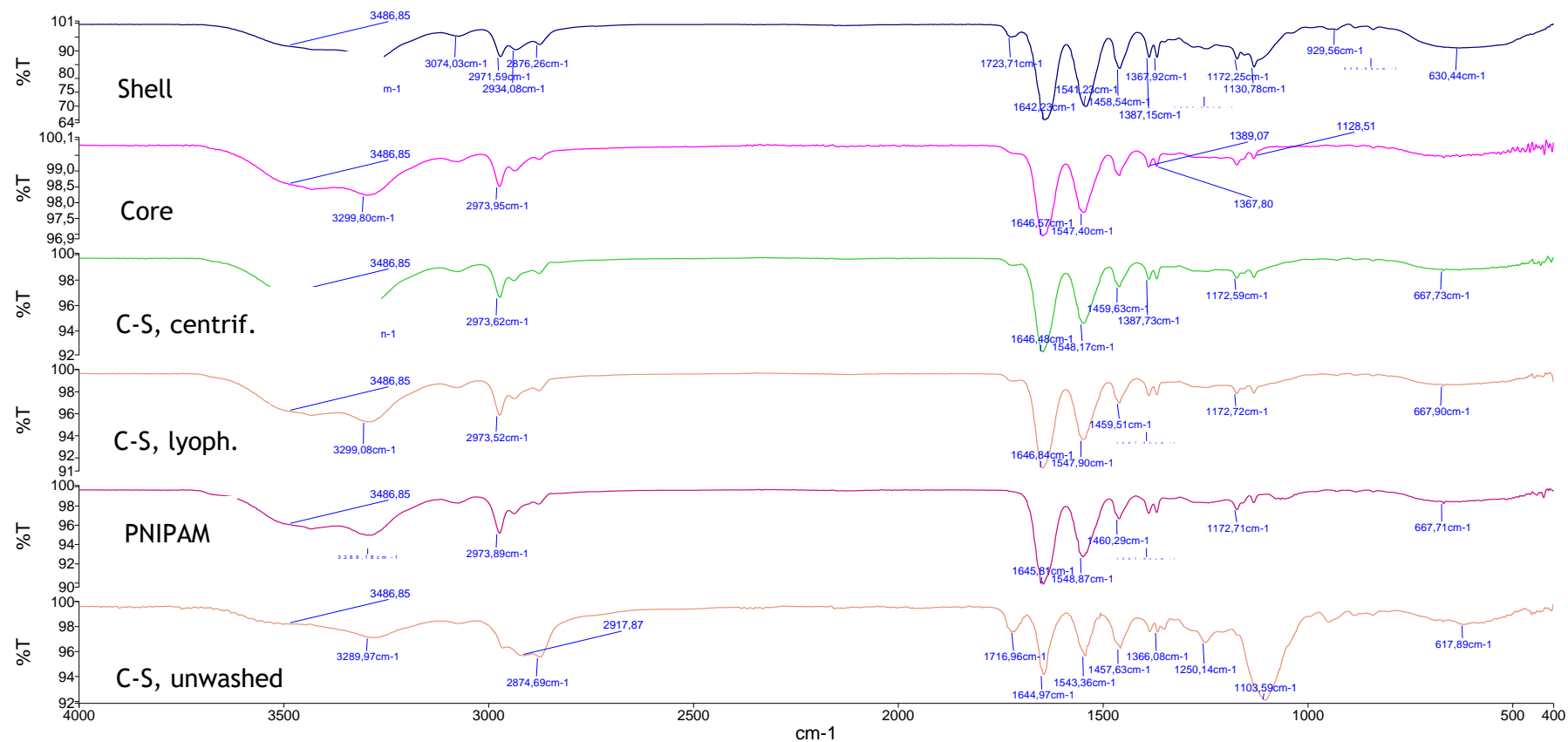## B.1. FTIR spectra of PNIPAM, core, shell, and core-shell microgels

Figure A. 3. Fourier transform infrared spectrogram of shell, core-shell (unwashed, centrifuged and lyophilized), core and PNIPAM microgels. Shell, core, and PNIPAM particles were centrifuged prior to this analysis. Vertical offset was adjusted for individual curve analysis.

Figure A. 4. Fourier transform infrared spectrogram of PEGMA. Notice the main peaks at 2871, 1250, 1718 and 1106 cm^{-1}.